Original Article

Experimental failure analysis and mechanical performance evaluation of fiber-metal sandwich laminates interleaved with polyamide-6,6 interlayers through the combined usage of acoustic emission, thermography and microscopy techniques

Bertan Beylergil[1], Isa E Tabrizi[2,3,5], Jamal SM Zanjani[4], Shaghayegh Saeidiharzand[2,3,5], Leila H Poudeh[2,3] and Mehmet Yildiz[2,3,5] [ORCID]

[1]Department of Mechanical Engineering, Alanya Alaaddin Keykubat University, Antalya, Turkey
[2]Integrated Manufacturing Technologies Research and Application Center, Sabanci University, Istanbul, Turkey
[3]Composite Technologies Center of Excellence, Sabanci University-Kordsa, Istanbul Technology Development Zone, Istanbul, Turkey
[4]Faculty of Engineering Technology, University of Twente, Enschede, The Netherlands
[5]Faculty of Engineering and Natural Sciences, Sabanci University, Istanbul, Turkey

Corresponding author:
Mehmet Yildiz, Faculty of Engineering and Natural Sciences, Sabanci University, Orhanli-Tuzla, Istanbul 34956, Turkey.
Email: meyildiz@sabanciuniv.edu

Abstract
Fiber-metal laminates are hybrid sandwich composite structures made of thin metallic sheets and layers of fiber-reinforced plastics. In this study, for the first time, the effects of polyamide 66 nonwoven interlayers on the tensile, three-point bending, interlaminar shear strength, and low velocity impact responses of fiber-metal laminates are investigated by coupling acoustic emission, thermography, and microscopy techniques. The fiber-metal laminates are interleaved with polyamide 66 nonwoven fabrics at two different areal weight density, namely, 17 gsm (grams per square meter) and 50 gsm. The tensile, bending, interlaminar shear strength, and low velocity impact tests are carried out in accordance with the ASTM standards. During the tensile and flexural tests, acoustic emission data are collected to understand damage types occurring under various loading conditions and, in turn, clearly shed light on the performance of polyamide 66 for interfacial strengthening in fiber-metal laminates. The results of acoustic emission investigation are correlated with the optical and scanning electron microscope-based microscopic analysis. It is shown that the interlaminar shear strength of fiber-metal laminates can be increased significantly (about 42%) by using polyamide 66 nonwoven interlayers. The impacted fiber-metal laminate specimens are examined to determine damage area and length using the lock-in thermography method. It is found that the polyamide 66 interlayers decrease the debonded length and damaged area up to 39 and 32%, respectively. The tensile and flexural strength and modulus of the fiber-metal laminate are not significantly affected by the presence of polyamide 66 interlayers, except a negligible drop in the value of tensile and flexural strength by 6 and 4%, respectively. The polyamide 66 interlayers are proved to be very successful in enhancing plastic deformation ability of the matrix and bonding efficiency between aluminum and composite sections.

Introduction

Fiber-metal laminates (FMLs) are hybrid sandwich composite structures made of thin metallic sheets and layers of fiber-reinforced plastics (FRPs) [1]. Reinforcing fibers in FML systems can be either glass, aramid, or carbon fibers, and the metallic constituent can be aluminum or titanium. FMLs are especially being used in aerospace applications such as in the lower wing skin and pressurized fuselage cabin where the fatigue performance is very critical [2]. The use of FMLs overcomes the drawbacks of each constituent: the poor fatigue strength of the

aluminum and the poor impact/residual strength of FRPs. Due to fiber bridging of the crack in the metallic layer, fatigue crack growth rates in FMLs are reported to be almost 100 times slower than that of aluminum [3]. Therefore, FMLs have received significant attention amongst researchers due to their better impact/ fatigue properties and fire resistance as compared to traditional metallic alloys and FRPs. However, FMLs are multi-phase interface systems, being rather prone to interfacial debonding by bending induced shear stresses [2]. The inter-laminar shear strength (ILSS) is one of the most significant mechanical properties that should be considered in the design of FMLs structures. Since the interface layer between the aluminum and composite section is not sufficiently strong, the ILSS of FMLs is in general lower than those of laminated composites [4].

Two comprehensive reviews on FMLs were published by Sinmazçelik et al. [5] and Chandrasekar et al. [6]. There are many published studies in the literature mainly focused on the impact and fatigue properties of FMLs, more specifically on the impact properties of GLARE (glass laminate aluminum-reinforced epoxy) laminates. Recently, Sadighi et al. [7] presented a review on the relevant literature which deals with experimental and numerical studies on the impact properties of FMLs. However, a few studies exist on investigating the other mechanical properties of FMLs such as tension, bending, compression, and ILSS. In the following, some of the recent studies on the in-plane and interlaminar shear properties of FMLs are summarized. Two recent studies by Sharma et al. [8] and Mathivanan et al. [9] focused on the uni-axial tensile response and failure of FMLs. They investigated the effects of aluminum thickness and fiber orientations on the tensile behavior of FMLs. Reyes and Cantwell [10] focused on the mechanical response of FMLs consisting of aluminum layers and glass fiber-reinforced polypropylene (PP). They observed that the load–displacement response was almost linear until the maximum load was reached, and then a sudden drop was observed due to the failure of composite layers. They also showed that the tensile strength increased linearly with composite volume fraction. Du et al. [11] investigated the open-hole tensile strength of carbon fiber-reinforced PEEK-titanium laminates both experimentally and numerically. Li et al. [12] studied bending failure mechanism and flexural properties of GLARE laminates with different stacking sequences. They showed that the bending failure of GLARE laminates includes several sequential steps, namely, elastic, plastic, and the local fracture of fiber layer and delamination. Hinz et al. [13] conducted a study on the damage characterization of GLARE laminates under interlaminar shear load. They employed a double-notch shear test (DNS) to investigate interlaminate shear properties and determined the ILSS of GLARE laminates as well as shear stress values corresponding to the onset of the fibre/matrix-debonding. Another study by Hinz et al. [14] investigated the damage mechanisms of GLARE laminates under interlaminar shear loading at different temperature conditions. They performed both ILSS and DNS tests. Liu et al. [15] investigated the interlaminar failure behavior of GLARE-3/2–0.3 laminates under short-beam load with various span length-to-specimen thickness ratios (L/h). They concluded that the short-beam shear test should be used as the main method for

determining the ILSS of FMLs, and shear dominant failure mode could be reliably obtained at the L/h ratio of 8 and below. Zheng et al. [16] also arrived at the same conclusion that shear stresses were dominant under the condition of low L/h ratio. As can be clearly inferred from the existing state of the art in literature, further studies are needed on the tension, bending, and shear properties of FMLs due to their growing applications in related industries.

Thermoplastic interleaving is one of the most promising techniques for improving mechanical performance of composite structures. In this technique, different interleaf materials in micro or nanoscale are placed between the interface of reinforcing plies to improve some of the critical mechanical properties of composites such as delamination and impact resistance. Two recent studies by Beylergil et al. [17,18] showed that PA 66 micro and nanofiber interleaving were very effective to improve delamination and impact resistance of carbon fiber/epoxy composites. Recently, Quan et al. [19] investigated the effects of polyethylene terephthalate interleaf material integrated with and without multi-walled carbon nanotubes on the electrical conductivity and fracture toughness of unidirectional carbon fibre/epoxy composite. Other interleaf materials such as polyvinyl alcohol nanofibers [20], aramid [21], and carbon fibers [22] were also studied in the literature. Although there are an increasing number of studies on this subject, the published studies focused mainly on the application of thermoplastic interleaving to traditional composite structures. Only three studies [4,23,24] focused on the effect of thermoplastic interleaving technique on the impact response of carbon/epoxy and GLARE laminates. Zarei et al. [4] reported that the PA 66 nanofibers were very effective to improve the mechanical performance (impact resistance) of GLARE laminates.

Damage occurrence and development inside the materials cause the release of energy in the form of acoustic waves or hits; therefore, collecting these acoustic hits through piezoelectric sensors can be used as major structural health monitoring tool. Specifically, failure in composite materials involves accumulation of various damage types, and clustering the corresponding AE hits can be helpful to understand the progressive failure of these materials [25]. Various studies have been conducted by investigators to cluster AE signals for composite materials [26–29]. Here, some of the efforts made by investigators are included. Tabrizi et al. [30] used K-means method to cluster AE data for glass/carbon fiber hybrid laminates under tensile and bending conditions, and their results revealed four different clusters each corresponding to a different failure. Bohmann et al. [31] clustered failure types in unidirectional glass fiber-reinforced laminates using K-means method, and their results revealed that change in loading condition does not vary the clustering results. Yilmaz and Yildiz [32] show in their investigation that the correct clustering of AE through K-means method can reveal the main micro-damages which correspond to reduction in Poisson's ratio. Despite numerous studies on fiber-reinforced laminates, very few studies are focused on AE analysis of sandwich composites and metal/fiber-resin structures. Pawar et al. [33] used AE system to analyze cutting mechanism in glare samples and showed direct relationship between AE absolute energy levels and delamination severity. Al-Azzawi et al. [34] used AE to show that

splice and doubler joints in glare laminates fail through different failure mechanisms under buckling load condition. Ammar et al. [35] used fuzzy C-means method to cluster AE data under four-point bending of E-glass/foam sandwich specimens. They have identified four clusters with an increasing order of amplitude level for core damage, resin cracking, interface debonding, and fiber rupture, respectively. Pashmforoush et al. [36] analyzed mode-I failure of glass fiber/epoxy-polyethylene foam sandwich composites. Their AE results indicated that frequency ranges between 35–65, 100–130, 170–250, and 350–450 kHz are related to core failure, debonding, matrix cracking, and fiber breakage respectively. They have signified that good adhesion between face sheets and core material can reduce acoustic hits in the frequency range of 100–130 kHz. Bussiba et al. [37] investigated GLARE samples under uniaxial mechanical loading and fracture toughness tests accompanied by AE analysis. They showed the effect of temperatures variation on failure modes of the interface of the metal/resin-fiber ply. Despite these studies, more work is required to delve into AE analysis of damage developments in FMLs and interleaving nonwoven fabrics. Furthermore, the partitioning clustering algorithms used have been mostly confined to center-based methods such as K-means and K-medoids. No density-based clustering algorithm measurements have been implemented for damage analysis in FMLs.

To the best of the authors' knowledge, the effects of PA 66 microfiber nonwovens on the mechanical performance of FMLs were not covered in the current literature. Although the effects of PA 66 nanofiber interleaving on the impact response of GLARE laminates were studied in the literature, there have been no studies done on the effects of PA 66 microfiber interleaving technique on the in-plane and out-of-plane mechanical properties of FMLs. This study aims to fill this research gap and clarify the effects of PA 66 nonwoven fabrics on the mechanical properties of FMLs. This is the first study in which the effects of PA 66 nonwoven fabric interlayers on the tensile, three-point bending, ILSS, and low velocity impact of FMLs are investigated. FMLs are made of thin aluminum sheets (2024-T3 Al clad) and 2×2 twill E glass/epoxy composite prepreg layers. FMLs are interleaved with PA 66 nonwoven fabrics at two different areal weight density: 17 and 50 gsm. All mechanical tests were carried out in accordance with the relevant ASTM standards. AE measurements are used to collect AE signals and damage propagation data during tensile and three-point bending tests. For the first time, AE technique is used to figure out the damage types in tensile loading of nonwoven fabrics separately. The fractured surfaces of reference and PA 66 interleaved FMLs are examined by using stereo microscope and scanning electron microscope (SEM) to interpret the failure modes and toughening mechanisms observed in the FML specimens under different loading conditions.

Materials

2024-T3 Alclad aluminum alloy sheets with a thickness of 0.8 mm are supplied by Seykoc Aluminum. Co, Turkey. According to the manufacturer's data, the

Table 1. Elemental composition of Al 2024-T3 sheets.

Fe	0.5
Si	0.5
Cu	3.8–4.9
Cr	0.1
Mn	0.3–0.9
Mg	1.2–1.8
Zn	0.25
Zi + Ti	0.15
Others	0.15
Al	Bal.

elemental composition of the aluminum sheets is shown in Table 1. The 2×2 twill E glass/epoxy prepreg layers (areal weight density: 210 gsm, 37 ± 3 wt% epoxy resin, and Product Name: KOM12 MET EGF TW 210) are supplied by Kordsa Inc., Turkey. The matrix material is hot-melt resin composed of structural epoxy resin, dicyandiamide hardener, and urone-based accelerator. The matrix is a toughened, 130°C cure epoxy resin with Young's modulus of 2.6 GPa, the tensile strength of 36 MPa, shear modulus of 974 MPa, elongation at break of 2%, and T_g of $\geq$130°C (data provided by the manufacturer).

The commercial PA 66 fabrics (N-Fusion^{TM}) at two different areal densities (17 and 50 gsm (grams per square meter)) are provided by Cerex Advanced Fabrics Inc., USA. These spun-bonded nonwoven fabrics are produced using a continuous filament process. In this study, the terms of interleaf and interlayers are used interchangeably. SEM images of the PA 66 nonwoven fabrics are shown in Figure 1. The fiber diameter is determined by measuring at least 25 fibers per sample using ImageJ software (National Institute of Mental Health, Bethesda, MD, USA). The average fiber diameter is determined as 19.94 ± 1.79 µm. The thicknesses of PA 66–17 and PA 66–50 gsm nonwoven fabrics are 80 and 150 µm, respectively.

Thermal analysis of PA 66 nonwoven fabrics

Thermogravimetric analysis (TGA) and differential scanning calorimetry (DSC) technique are used to determine the degradation, melting, and glass transition temperature of the PA 66 nonwoven fabrics by Mettler Toledo TGA DSC + 3. Figure 2 shows the DSC and TGA curves of the PA 66 nonwoven fabrics. In TGA analysis, the samples are heated from room temperature to 1000°C at a heating rate of 10°C/min under nitrogen atmosphere. The degradation temperature is determined as 394°C. In DSC analysis, the samples are heated from room temperature to 350°C at a heating rate of 10°C/min under nitrogen atmosphere. The melting and glass transition temperature of the PA 66 nonwoven fabrics are determined as 256 and 87 °C, respectively. DSC and TGA analyses clearly indicate that
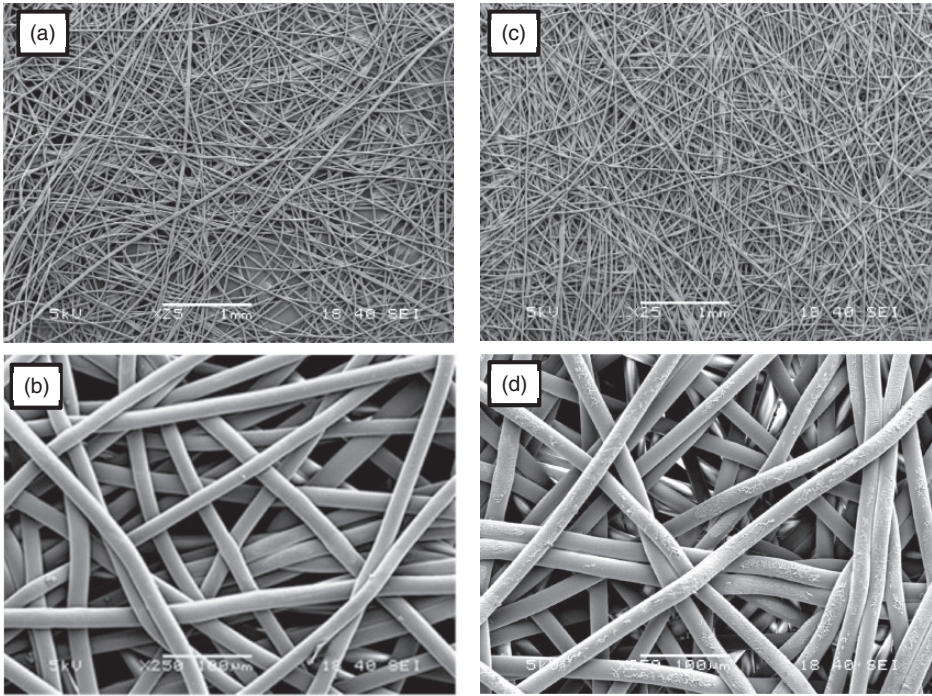
Figure 1. SEM images of (a,b) 17 gsm and (c,d) 50 gsm PA 66 nonwoven fabrics.

the PA 66 microfibers retain their structure in the FMLs since the curing temperature is much lower than the melting and degradation temperature of PA66 nonwoven interlayers.

Manufacturing of FMLs

Reference and PA 66 nonwoven interleaved FMLs are manufactured by hot-pressing technique. The atmospheric plasma treatment is performed on the surface of aluminum sheets before the stacking of the FMLs constituents (Figure 3). The RD1004 plasma rotary nozzle is used to generate cold plasma. The plasma distance and speed are 10 mm and 50 mm/s, respectively. Reference FMLs are manufactured by stacking of eight 2×2 Twill E-glass/epoxy prepreg layers between 2024-T3 Alclad aluminum alloy sheets. The balanced E-glass prepregs were cut in the roll direction and placed parallel to the edges of the aluminum sheets. Then, the heat (120°C, 60 min) and pressure (6.4 bars) are applied simultaneously to the stack, which is then left to cool at room temperature. To produce PA 66 interleaved FMLs, two different types of PA 66 nonwoven fabrics (areal weight densities: 17 and 50 gsm) are placed between the aluminum and prepreg layers.
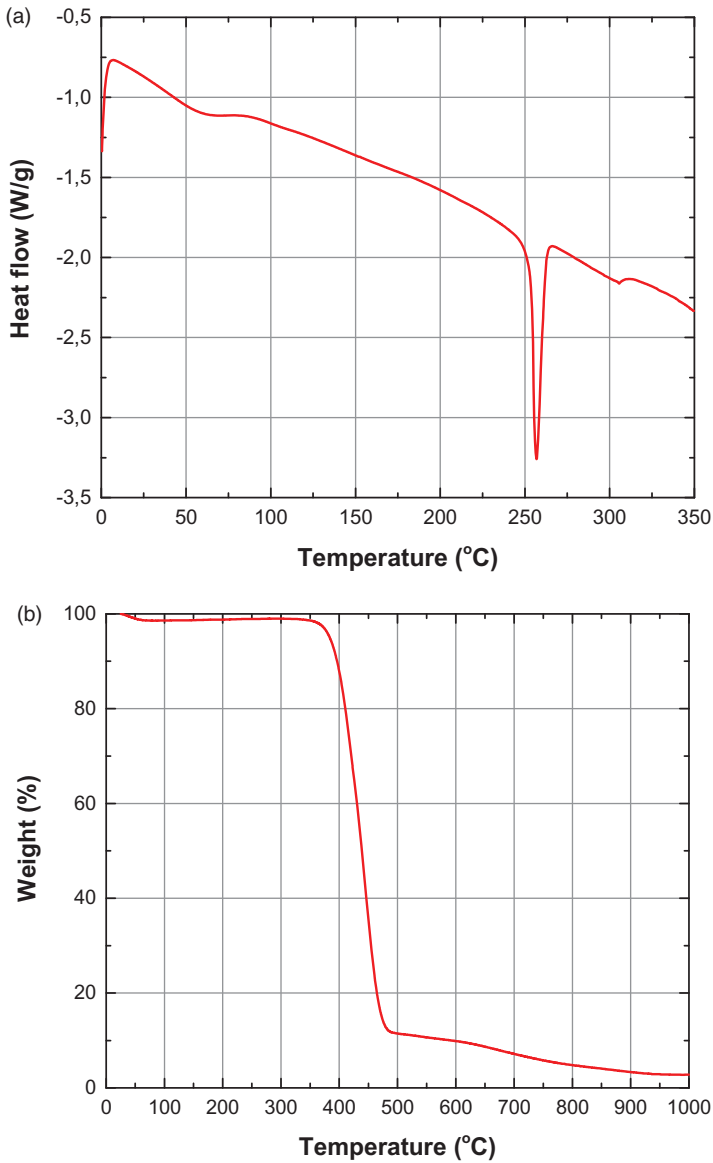
Figure 2. (a) DSC and (b) TGA curves of the PA 66 nonwoven fabrics.

A schematic representation of the FMLs with their sample codes is shown in Figure 4. The average thickness of the reference FML, 17-FML and 50-FML specimens is determined as 2.97, 3.06, and 3.12 mm, respectively. The incorporation of 17 and 50 gsm PA 66 nonwoven fabrics results with an insignificant weight
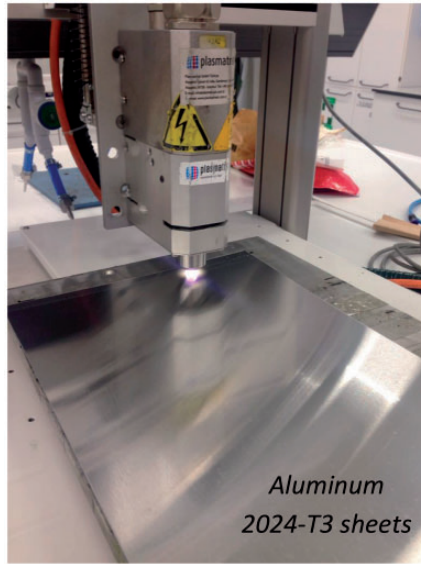
Figure 3. Open air plasma treatment of aluminum surfaces.

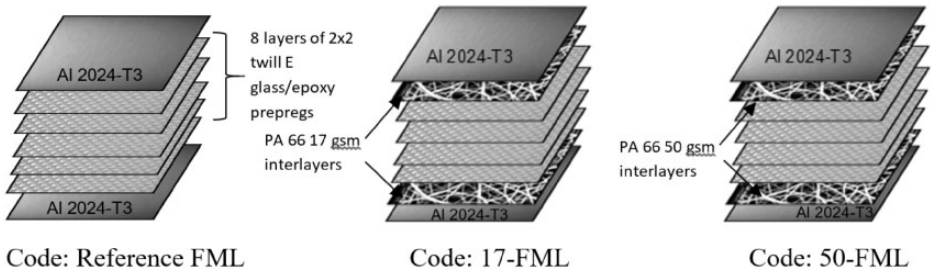Code: Reference FML   Code: 17-FML   Code: 50-FML

Figure 4. Schematic representation of reference and PA 6,6 interleaved FMLs.

penalty, so that 17 and 50 gsm PA 66 nonwoven fabrics increases the overall weight of FMLs by about 0.5 and 1.5%, respectively.

Mechanical tests

All mechanical tests are performed using universal testing machine by Instron with the model number of 5982 at room temperature in accordance with the relevant ASTM standards [38–40]. At least five specimens for each test are tested at the room temperature, and the average results are reported in this study. The tensile tests were carried out at a constant crosshead speed of 2.0 mm/min. A clip-on extensometer with knife edges is used to measure the strain until the total failure
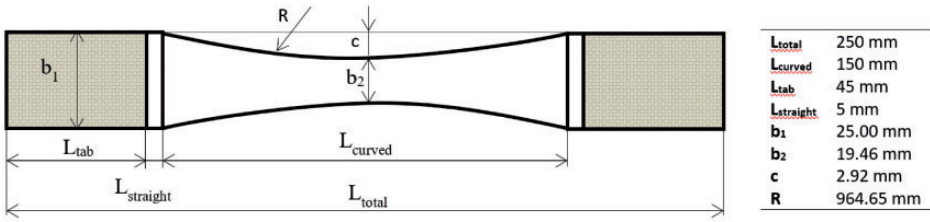
Figure 5. Geometry of a dumbbell-like shape tensile test specimen.

of the specimen occurs. Figure 5 shows the geometry of the tensile test specimens used in this study. Instead of using a rectangular geometry, the specimens are cut into the dumbbell-like shape by waterjet system, thereby preventing premature failure of the specimen in the gripping regions and promote a failure within the gauge length of the extensometer under the loading. The gripping regions are wider than the gauge section which causes a stress concentration in the midsection of the specimen. This stress concentration ensures a higher likelihood of failure away from the gripping ends. The stress concentration factor, the ratio of b_1/b_2, is calculated as 1.30 due to the curved length in the specimens. A detailed information about the geometry of the tensile specimens can be found in De Baere et al. [41,42]. The flexural properties of the reference and PA 66 interleaved specimens are obtained from three-point bending tests. A span-to-thickness ratio of 16:1 is used on the test fixture. The test speed is 1.0 mm/min. ILSS tests are determined using the short beam shear test. A span-to-thickness ratio of 2:1 is used with a span of 12 mm on the test fixture. The crosshead speed is 1.0 mm/min.

Low-velocity impact tests are performed with a drop weight impact testing machine CEAST 9350. The length and width of the FML specimens are 150 mm × 100 mm, respectively. The specimens were held with the clamp fixture placed under the impactor. The dropping weight is 6.62 kg. The impactor end is a hemispherical-shaped tube having a diameter of 12.7 mm. To conduct the impact test, drop height of impactor is determined as 229.0 mm to strike samples at nominal energy levels of 60 J. Transient response of the specimens such as velocity, deflection, energy, and force is recorded as a function of time for each specimen. Impact response of FML specimens is analyzed through the average of load, energy, and time data. For each group of FML specimens, three samples are tested at 60 J energy level. After impact tests, the FML specimens are cut into two halves through the midplane by using a waterjet cutter. The debonded length of the specimens is measured by using Image J software.

To determine the damage area of impacted specimens, lock-in infrared thermography technique is used. Infrared thermography camera is FLIR X6580sc with a cooled photon detector (indium antimonide) and 25 mm lens. This camera has a maximum resolution of 640 × 512 pixels at 355 Hz. The resolution decreases as the frame rate of data acquisition increases. The images taken in thermography had a spatial resolution of 640 × 512 pixels. The distance between camera and specimen

is set to 600 mm to have enough depth of field and obtain the appropriate focus level. Sinusoidal wave is generated using HEDLER LED lamps with frequency of 0.01 Hz while recording the thermal response of FMLs with thermal camera at frame rate of 50 Hz. The evaluation of attained images is accomplished using Edevis DisplayImg 6 software based on Fourier transformation. The phase variation images from the surface of samples are prepared to compare the size of damaged area after impact tests. The samples are painted in black for better absorption of heat during thermal imaging and prevent high reflectivity and emissivity of aluminum. Figure 6 shows the photographs of the tensile, three-point bending, ILSS, and low-velocity impact test specimens.

Acoustic emission experimental procedure

Acoustic emission (AE) monitoring and data analysis are conducted using Mistras PCI-2 system. Two AE sensors of PICO type with operating range of 200–750 kHz and resonance frequency of 550 kHz are attached to the surface of tensile and flexural samples (please refer to Figure 6). The distance between the sensors is 60 and 40 mm, respectively, for tensile and flexural cases. The burst of energy (acoustic hits) during micro damage formation and/or propagation inside laminates is sensed as a time domain waveform. These waveforms are amplified using Mistras 0/2/4 preamplifiers with 20 dB gain. Threshold for data recording is set to 45 dB to ensure no noise footage in the availed data. Timing parameters for acoustic signals are set to 50-μs peak definition time, 150-μs hit definition time, and 300-μs hit lockout time. The sampling rate of AE is set to 2 MHz; moreover, strain value for each acoustic hit is obtained utilizing an analog voltage from tensile test machine. Collected AE data after mechanical tests is filtered using a Bessel bandpass filter of the order 8 between 20 and 800 kHz. Main features of acoustic hits are extracted which include both time domain and frequency domain properties.

To find out the AE characteristics of PA 66 nonwoven fabrics under tensile loading, three samples from each nonwoven fabric, i.e. 17 and 50 gsm, are cut into size of 250×25 cm with 150 mm gauge length. The ends of the specimens are then tabbed using double-sided adhesive tapes to prevent their failure at tensile machine grips or possible slip through machine jaws. An AE sensor identical to the ones used for mechanical tests of FMLs is used. The sensor is adhered at the center of gauge length using hot melt adhesive. Since the test material is a non-rigid medium, the possibility of efficient data recording during tensile loading is reduced. To solve this problem and make sure that the valuable data will be obtained, the failure region of the sample is predetermined through implementation of two side notches at both edges of the sample with length of 3 mm each. These edge cracks act as stress concentration regions and ensure that failure will propagate between these two notches or near them. Moreover, the crack propagation path will cross through or near the sensor adhesion point which secures reliable trace of AE data (Figure 7). For these tests, the same AE apparatus is used with only differences in the threshold and preamplifier gain values which are set to 30 and 40 dB,
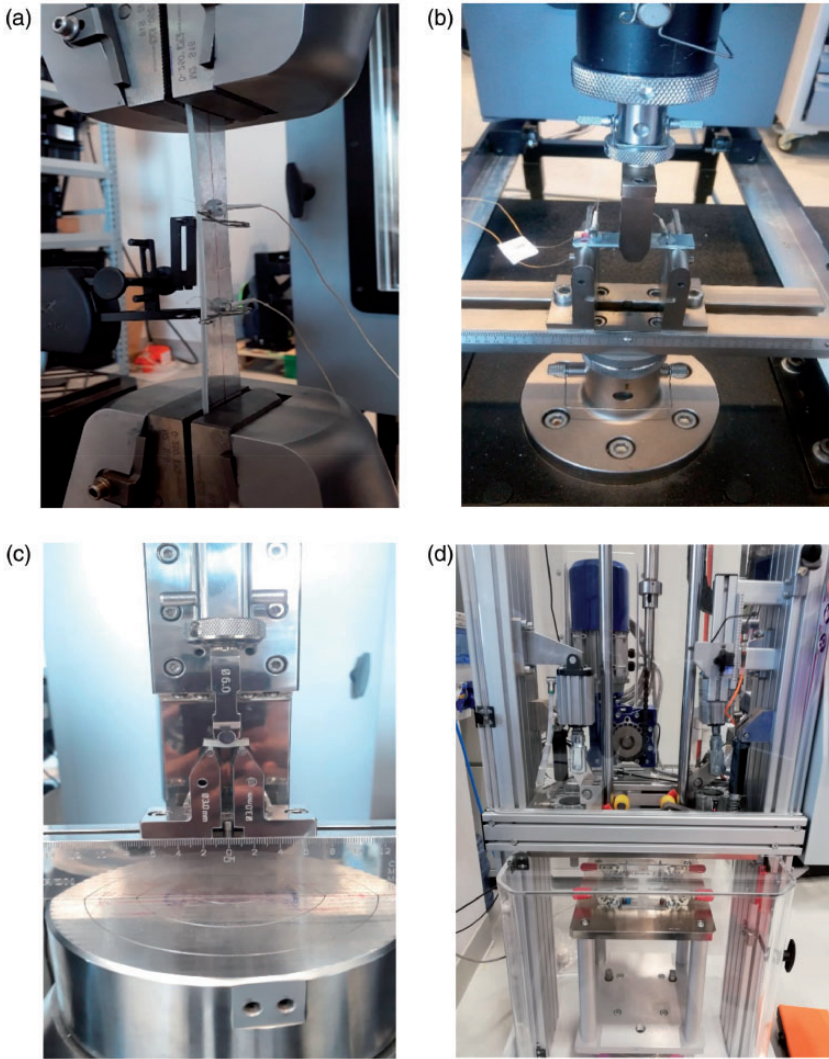
Figure 6. Photographs of the FML (a) tensile, (b) three-point bending, (c) ILSS, and (d) low-velocity impact test specimens.

respectively. Tensile test speed is set to 10 mm/min, i.e. displacement control, using the same universal test machine. For consistency, the post processing of AE data is performed considering the previous tension test set-up. A considerable amount of background noise is removed from dataset as the threshold of data acquisition was set to a low value of 30 dB. Moreover, any form of continuous waveform is removed to ensure analysis of only transient waves which are a characteristic of
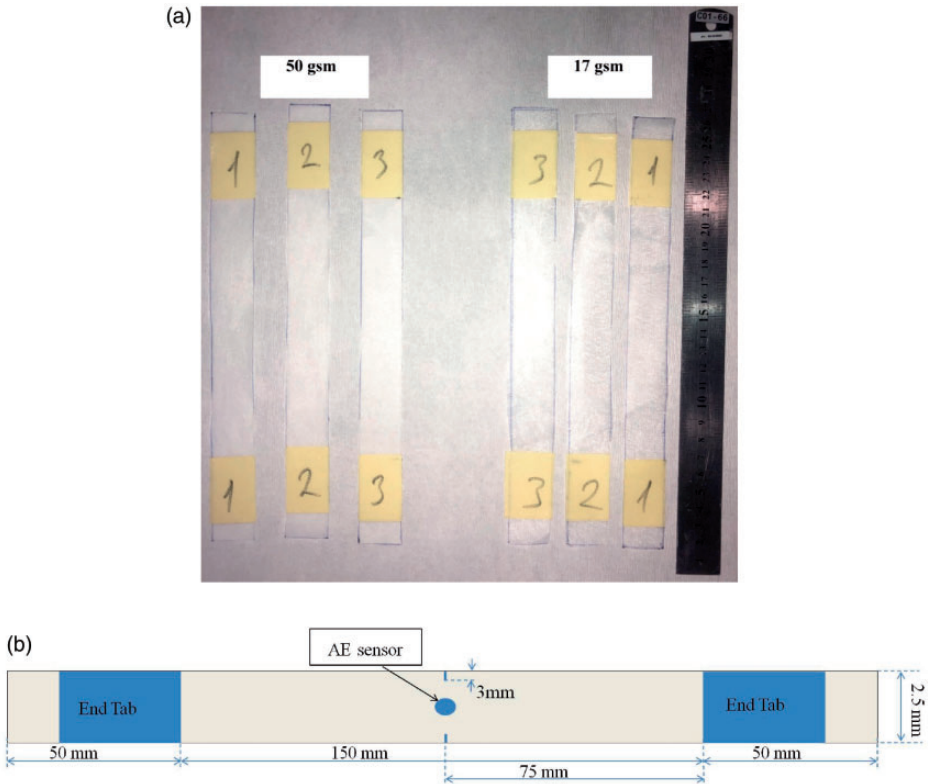
Figure 7. (a) PA 66 nonwoven fabric tensile test specimens and (b) schematic representation of sensor position and edge notch size for acoustic emission.

AE hits. Eventually, total number of acceptable waveforms from each sample decreases to a handful of data point.

The obtained AE hits under bending, and tensile loads are clustered using density-based spatial clustering of applications with noise (DBSCAN). This algorithm is based on the notion that for each point of a cluster, there must be a minimum number of neighborhoods datapoints (minpts) at certain radius (ε) [43]; therefore, outlier data points can be disregarded, and any shape of clusters at multidimensional space can be distinguished [44]. To perform DBSCAN algorithm on obtained acoustic data, weighted peak frequency and partial power 3 are selected as the appropriate acoustic features as discussed in a previous study by Tabrizi et al. [30]. The value of minpts is supposed to be greater or equal to one plus the size of vectors in feature space, i.e. minpts $\geq$ number of AE data points. To select the value of ε, graph of k-distance for input features is obtained using MATLAB function, and the knee of this graph is chosen as the appropriate choice of neighboring radius [43].

Results and discussion

Mechanical test results and fractured surface observations

Figure 8 shows the representative stress–strain curves of the FML specimens under tensile loading. As expected, the stress increases linearly with the strain at the initial stage, and then, the slope of the curves starts to decrease when the stress level reaches up to nearly 160–170 MPa. This nonlinear region is associated with the yielding or the plastic deformation of aluminum face sheets. When the stress levels reach their maximum values at which the composite sections fail in a catastrophic manner with a bursting sound (as seen in "AE test results" section) followed by sudden drops in stress levels. Glass fiber breakage and debonding between aluminum and composite sections occur simultaneously. After this point onward, only aluminum face sheets continue to carry tensile loads, and the stress levels start to increase gradually until the complete failure. It can also be noticed that the general trend of load–displacement curves is almost same for all group of the specimens. This is due to the fact that the response of the tensile specimens is mostly dominated by aluminum layers and reinforcing fiber properties. Although the matrix properties are changed due to the presence of PA 66 nonwoven fabrics which will be shown later, the tensile properties are not significantly affected by the altered matrix properties. On the other hand, some differences are observed in the failure modes of the tensile specimens. Figure 9 shows the
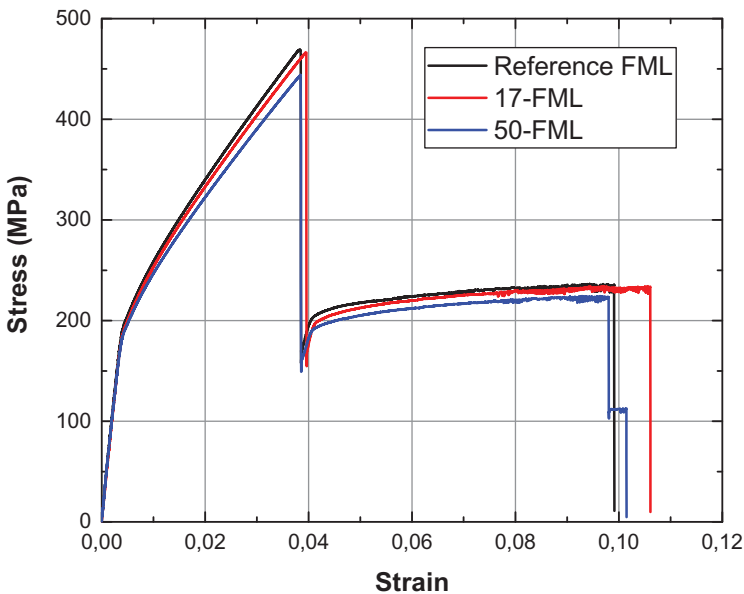

Figure 8. Representative stress–strain curves of the FML specimens under tensile loading.

failed test specimens under tensile loading. The failed specimens are analyzed by ImageJ software version 1.50b to determine the fracture angle of aluminum layers. For reference-FML and 17-FML, the aluminum layers are broken in the middle section of the specimens with an angle of about 65° with respect to the load direction. This is due to the motion of dislocations on the related slip plane of the crystal structure [45]. The reference FML specimens behaved similarly to those reported in the literature [8,9,45]. On the other hand, 50-FML specimens show different final failure as compared to the reference FML and 17-FML specimens. Some 50-FML specimens fail with a degree of 90° with respect to the loading direction while other 50-FML specimens break into two pieces with a combination of 90° and 65° with respect to the load direction. The incorporation of 50 gsm PA 66 interleaves between aluminum and composite section results in significant change in the response of FMLs under tensile loading. This mixed failure mode clearly bespeaks that PA 66 interleaves change the load transfer and energy absorption capacity of FML composites, which will be further elaborated in the coming sections of this study. Figure 10(a) to (c) shows the micrographs of reference FML specimens under tensile loading. The composite section of the reference FML specimens exhibits catastrophic failure with fiber breakage and delamination. Plastically deformed aluminum sheets can also be seen in Figure 10(a).
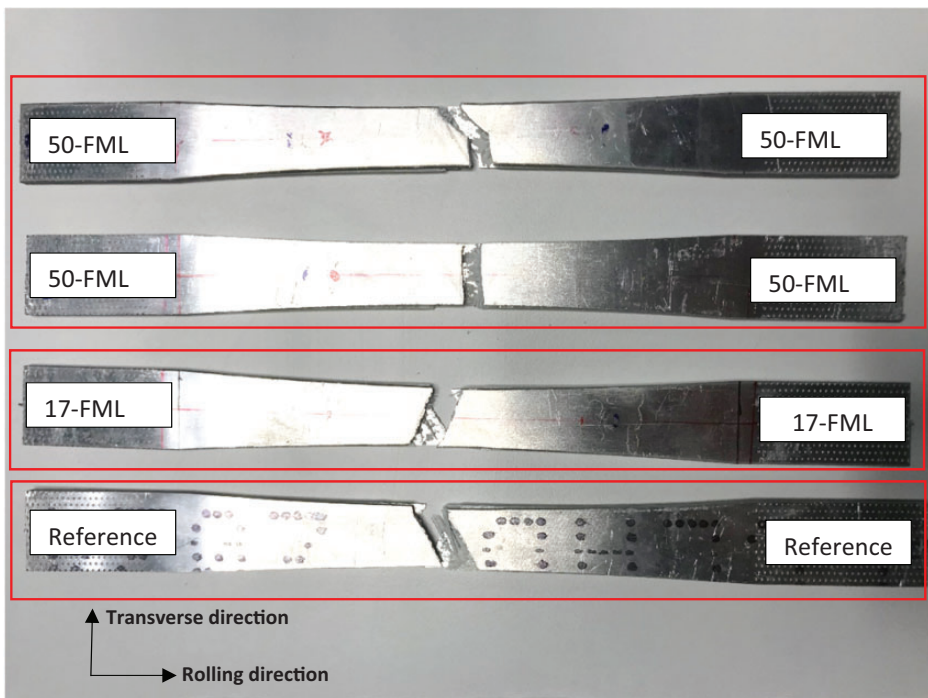

Figure 9. Failed reference FML, 17-FML, and 50-FML tensile test specimens.

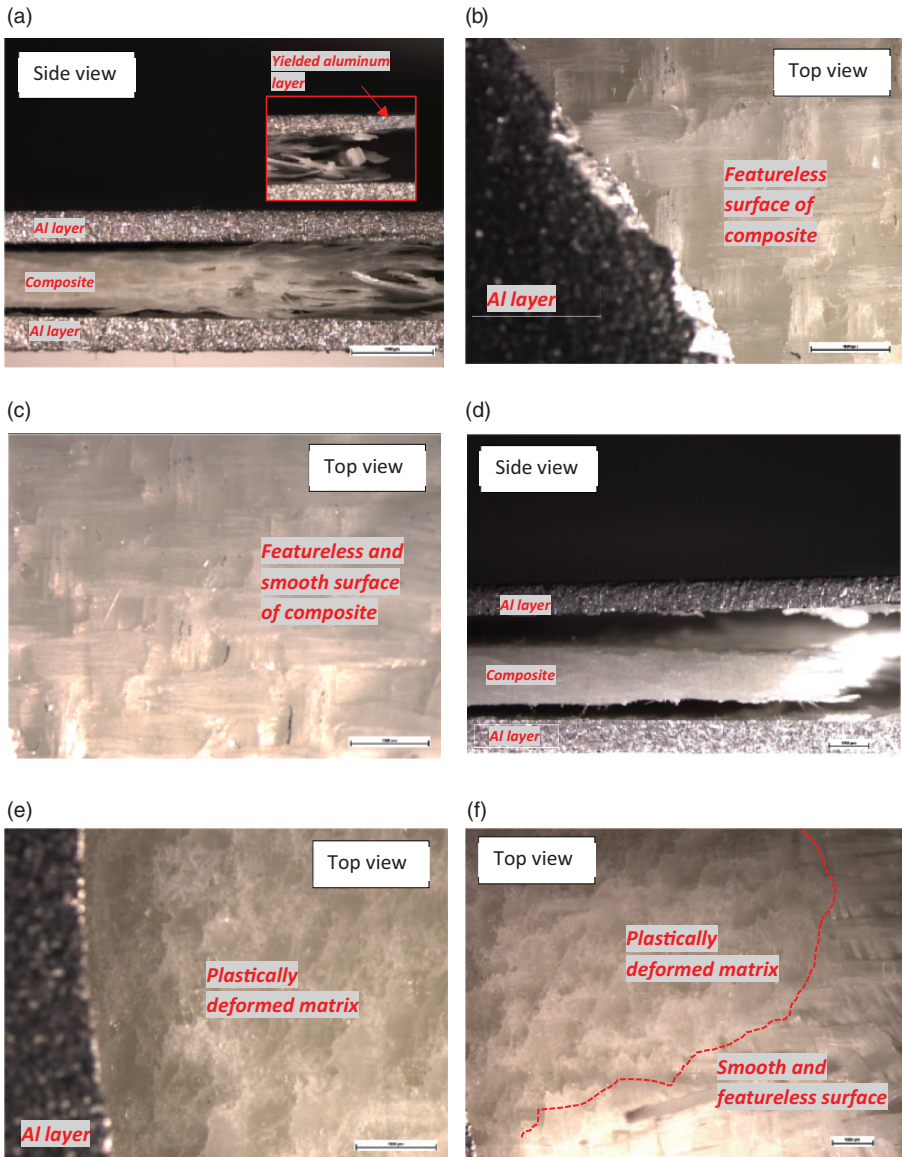**Figure 10.** Microscopic analysis of reference FML (a, b, c) and PA 66 interleaved FML (d, e, f) tensile test specimens.

The top view of reference FML specimens (Figure 10(b) and (c)) shows brittle nature of epoxy matrix, given that the surface is smooth and featureless without any sign of notable plastic deformation. Figure 10(d) to (f) shows the micrographs of PA 66 interleaved FML specimens. Compared to reference FML specimens, the

failure of PA 66 interleaved FML samples (Figure 10(d)) appears to be less catastrophic with less amount of delamination and fiber breakage, and the composite layers remain intact and continue to carry tensile loads with higher strain values. The top view of the PA 66 interleaved FML specimens is shown in Figure 10(e) and (f). Two different regions can be seen in these figures: (i) smooth and featureless (brittle) and (ii) more-ductile regions. It can be said that the PA 66 microfibers improve ductility and promote plastic behavior of the epoxy matrix through the formation of semi interpenetrating polymer network (semi-IPN) structure [46]. The tensile properties of FMLs decrease with the addition of PA 66 nonwoven fabrics due to the following reasons: first, the average thickness increases; second, the ductility of matrix increases; and last, the fiber volume fraction decreases in the resulting structure.

Figure 11 shows the SEM images of tensile specimens of PA 66 interleaved FMLs. The deformed and pulled-out PA 66 microfibers from the epoxy matrix can be seen in Figure 11(a) and (b), respectively. The severe matrix deformation can also be seen in these figures. Figure 11(c) shows highly oriented shear cups which proves the effective load transfer from aluminum to E-glass fibers through matrix due to the PA 66 microfibers.

The average elastic modulus and tensile strength of reference FML specimens are determined to be as 49.03 ± 0.80 GPa and 476 ± 9.13 MPa, respectively. The elastic moduli of 17-FML and 50-FML specimens are obtained to be as 49.0 ± 0.64 and 48.4 ± 0.44 GPa, respectively. As expected, there is no statistically significant change on the elastic modulus of the FML specimens after the incorporation of PA 66 interlayers between aluminum and composite section. This can be associated with the fact that the elastic modulus of the FMLs is controlled by composite section and aluminum layers. On the other hand, the tensile strength decreases negligibly from 476 MPa to 458 ± 9.13 MPa for 17-FML specimens, corresponding to 3.8%. The addition of denser PA 66 microfibers caused slightly higher reduction in the tensile strength, namely, 6.7%, such that the tensile strength of 50-FML specimens decreases from 476 to 444 ± 9.13 MPa. The drop in tensile strength is related to increased thickness of FMLs after the incorporation of PA 66 interleaves. The use of excessive amount of PA 66 interleaves on the aluminum/composite interface also results in premature failure. Also, PA66 nonwoven interlayers keep some part of the epoxy resin that should be thrown out from the prepreg during the curing cycle. This phenomenon causes the formation of enriched matrix interfaces which in turn reduce the strength of the FML.

Figure 12 shows the representative stress–strain curves of the FML specimens under flexural loading. The stress increases linearly with strain at the early part of the experiment. At this initial stage, both aluminum and composite section deform elastically until the stress level reaches 350 MPa approximately. As the strain is increased, the aluminum layer starts to yield and deforms plastically. The curve starts to deviate from linearity at this point while the composite section continues to deform in an elastic manner. After some displacement, stress level reaches a critical value in the composite section leading to the formation of microcracks.

(a)

(b)

(c)

(d)

(e)

(f)

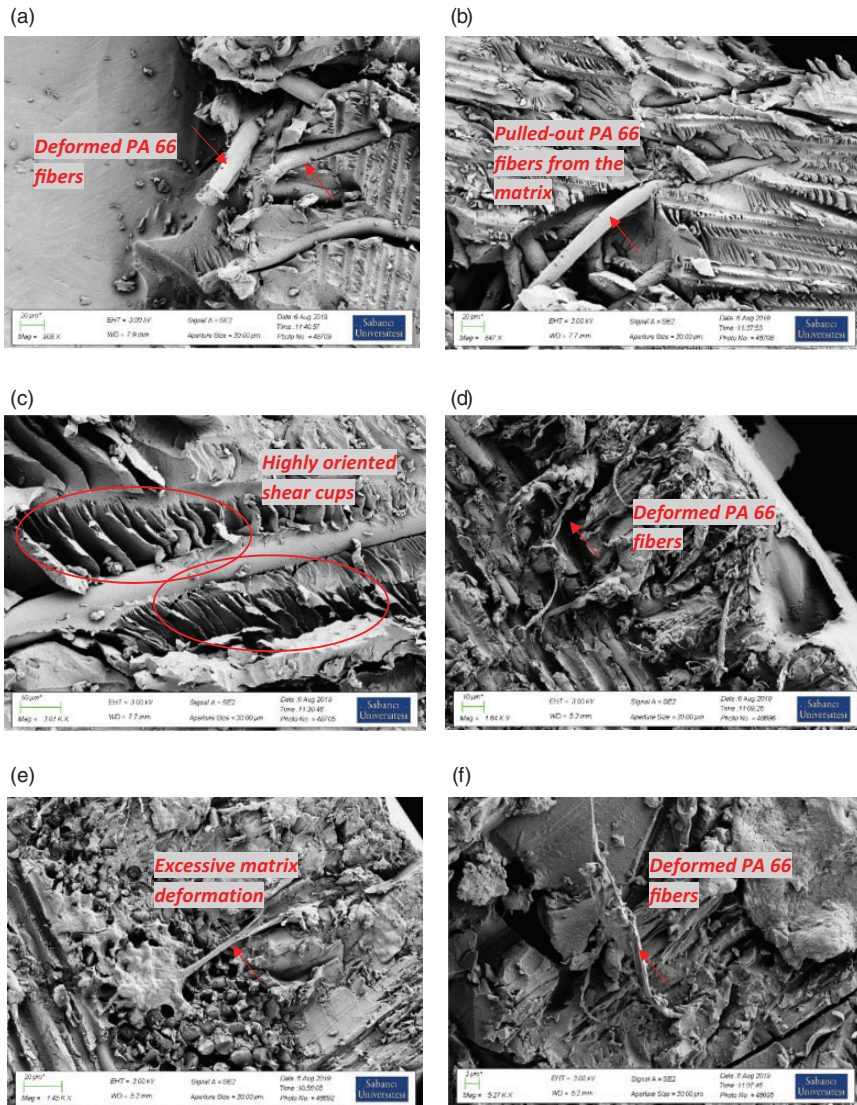**Figure 11.** SEM images of fractured surfaces (a–c) tensile and (d–f) ILSS specimens of PA 66 interleaved FMLs.

With the local fiber fracture, the stress levels decrease, and final failure takes place in the aluminum layer at the end of the experiment. The same behavior is also observed for the PA 66 interleaved composite specimens. The average flexural modulus and flexural strength of reference FML specimens are determined to be
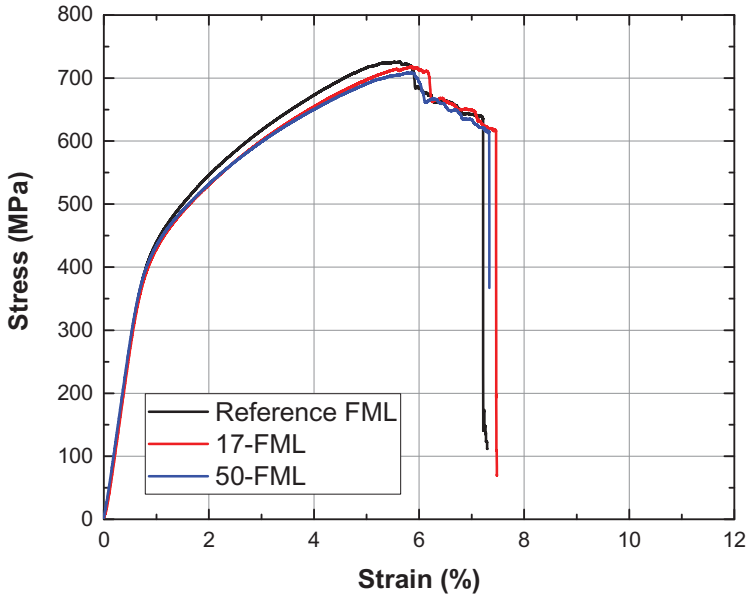
Figure 12. Representative stress–strain curves of the FML specimens under three-point bending.

33.03 ± 0.40 GPa and 731 ± 14.71 MPa, respectively. The flexural modulus of 17-FML and 50-FML specimens is obtained to be 32.55 ± 1.36 and 31.06 ± 1.22 GPa, respectively. As in the case of tensile testing, there is no significant change on the flexural modulus of the FML specimens due to the presence of the PA 66 inter-layers, given that the flexural modulus of the FMLs incorporates elastic properties of aluminum and composite section. However, the flexural strength decreases from 731 to 709 ± 9.09 MPa for 17-FML specimens. The use of denser PA 66 interlayers causes higher reduction, so that the flexural strength decreases from 731 to 702 ± 9.93 MPa for 50-FML specimens. This corresponds to a decrease for about 3.0 and 4.0% for 17-FML and 50-FML specimens, respectively. As compared to the tensile test results, the flexural strength values are reduced to a lesser extent due to the PA 66 interlayers. This observation can be related to higher dependence of flexural strength to the interface features, epoxy properties, and/or bonding between the layers of the composite section.

Figure 13 shows the micrographs of reference FML, 17-FML, and 50-FML three-point bending specimens together with the failure modes. One can clearly see the damage modes which include aluminum failure, fiber failure, matrix crack-ing, composite delamination, and composite/aluminum interface debonding. These failure modes are also reported by Li et al. [12], Rajkumar et al. [45], and Khalili et al. [47]. By comparing Figure 13(a) and (d), PA 66 interleaved specimens show less interface debonding compared to reference FML specimens. The interface
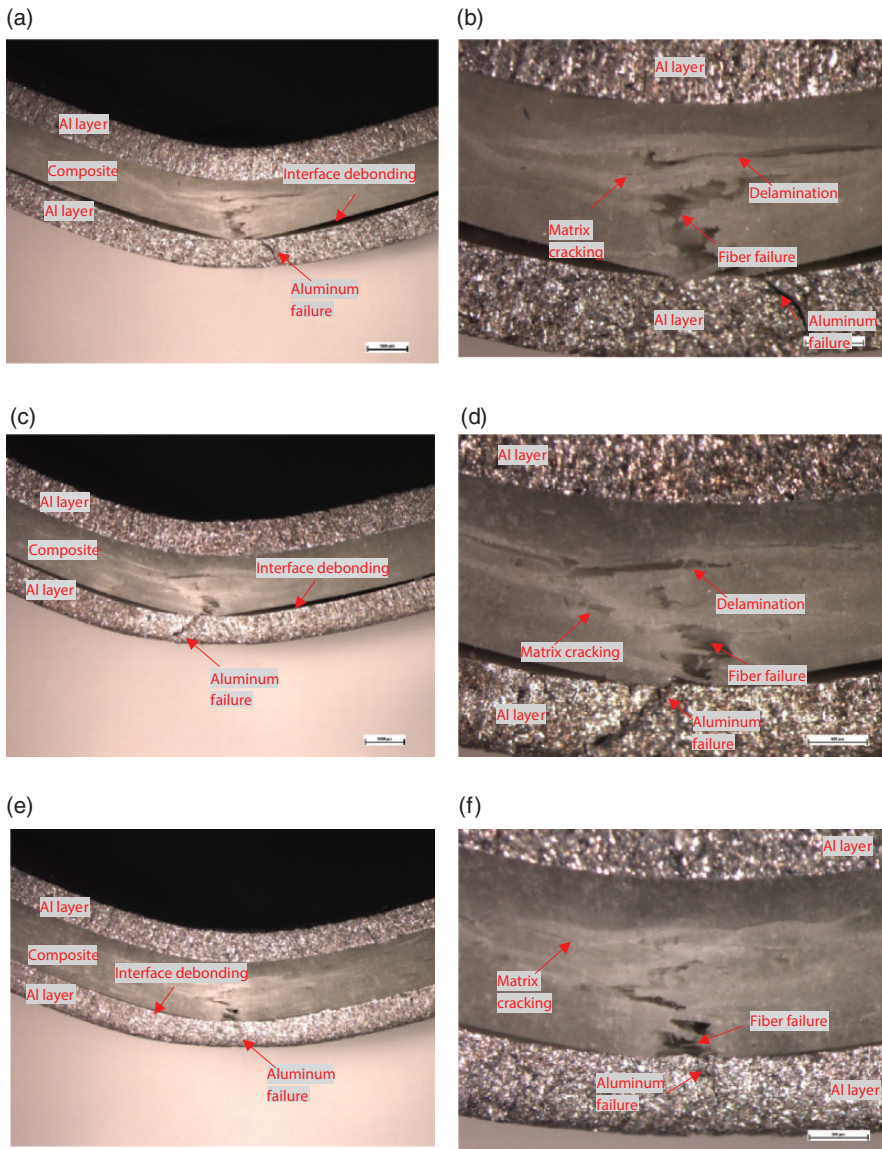
Figure 13. Microscopic analysis of (a, b) reference FML, (c, d) 17-FML, and (e, f) 50-FML specimens under three-point bending.

debonding area is significantly reduced after the addition of PA 66 microfibers. The denser PA 66 interlayers lead to higher reduction in debonded area between aluminum and composite section. At the same magnification level, 50-FML specimens show limited interface debonding area as compared to the other specimens.
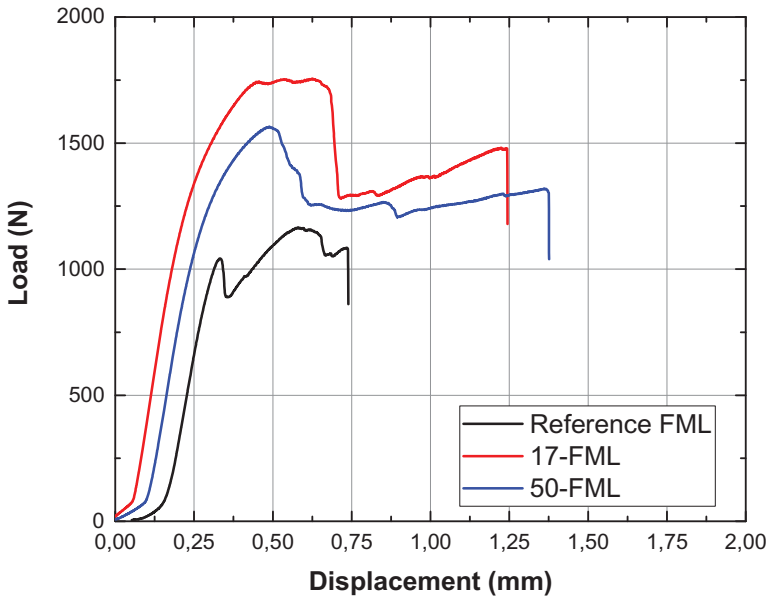
Figure 14. Representative load–displacement curves of the ILSS–FML test specimens.

Therefore, it can be said that the incorporation of PA 66 interlayers leads to significant improvement on the bonding efficiency of aluminum and composite sections. It is also important to note that with the use of PA 66 interlayers between aluminum and composite section of FML, the risk of composite section delamination is reduced (refer to Figure 13(b) and (f)). One would easily notice that smaller delaminated area is observed in the 50-FML specimens after the incorporation of PA 66 interlayers as compared to that of reference specimens.

Figure 14 shows representative load–displacement curves of short-beam (ILSS) FML specimens under flexural loading. For the reference FML specimens, the slope of the load–displacement curve is constant up to the load level of 1000 N and starts decreasing until the load reach its maximum value, and thereafter, the load experiences a steep descent due to the interface debonding between aluminum and composite section. In what follows, the load continues to increase with a relatively shallower slope to overcome interface bonding forces. The debonding starts from one of the edges of the reference FML specimens and propagates through the center of the specimens. After the debonding due to the transverse shear stresses, laminates are in the state of inelastic deformation which is one of the typical failure modes stated in ASTM standard [38]. Figure 14 also shows the load–displacement curves of 17-FML and 50-FML specimens, where one can see that the initial slope of curves is almost the same as the reference FML. However, it is obvious that the presence of PA 66 interleaves alters the response

of reference FML specimens. After the maximum load of the reference specimens is reached, the PA 66 interleaved laminates continue to carry further loads as compared to reference specimens since the PA 66 interlayered laminates continue to resist shear stresses during the loading. The denser PA 66 interlayers provide much higher displacement capacity before complete failure. The higher load bearing capacity of PA 66 interleaved FMLs accompanied by the higher displacement value bespeaks that 17-FML and 50-FML specimens possess better shear resistance as compared to reference FMLs. It is known that ILSS is a matrix-dominated property. Therefore, it can be said that the presence of PA 66 nonwoven fabrics alters the matrix properties which will be discussed in the following paragraphs.

Figure 15 shows the microscopic view of the fractured ILSS FML test specimens. As can be seen in Figure 15(a) and (b), the global failure of reference FML specimens is the combination of three different failure modes: (i) the interface-debonding between aluminum layer and composite section, (ii) inelastic deformation of composite section, and (iii) micro-buckling of aluminum face sheet. Two different failure modes, local buckling failure of aluminum layer and interface debonding, are observed in the 17-FML specimens as shown in Figure 15(b) and (c). No significant inelastic deformation of composite section is observed in these specimens. Some PA 66 fibers were noticeable between the aluminum layer and composite section (Figure 15(b) and (c)), and these PA 66 fibers act like bridging elements between aluminum layer and composite section. In the 50-FML specimens, interface debonding and inelastic deformation of composite section with a small and individual delamination are observed as shown in Figure 15(d) to (e). Although the interface debonding is observed on the top of the laminate, there was no sign of interface debonding on the bottom of the FML unlike the other specimens. It can also be seen in Figure 15(d) and (e) that some portions of composite layer remain bonded to the aluminum surface after loading. This proves that the presence of PA 66 interlayers increases the bonding efficiency between aluminum layer and composite section.

Figure 16 shows the average apparent ILSS values of FML specimens with/without PA 66 nonwoven interlayers. The ILSS of the reference FML specimens is determined as 48.45 ± 0.31 MPa. This result is consistent with the previous result reported by Botelho et al. [48]. On the other hand, the ILSS of the PA 66–17 and PA 66–50 gsm interleaved specimens are determined as 68.18 ± 1.86 MPa and 62.73 ± 1.16 MPa, respectively. It is obvious that the incorporation of 17 gsm PA interlayers leads to a significant increase in the ILSS by about 41%. The addition of denser 50 gsm PA interlayers also increases the ILSS about 30% but not as much as 17 gsm PA interlayers. This can be attributed to the increase of final thickness due to the denser PA interlayers. The higher ILSS for PA66 interleaved FMLs indicates better composite/aluminum adhesion than reference laminates, which proves a more efficient load transfer from aluminum to composite section and consequently a better structural behavior. The improved shear performance can be attributed to the bonding between the amide groups of nylon and the

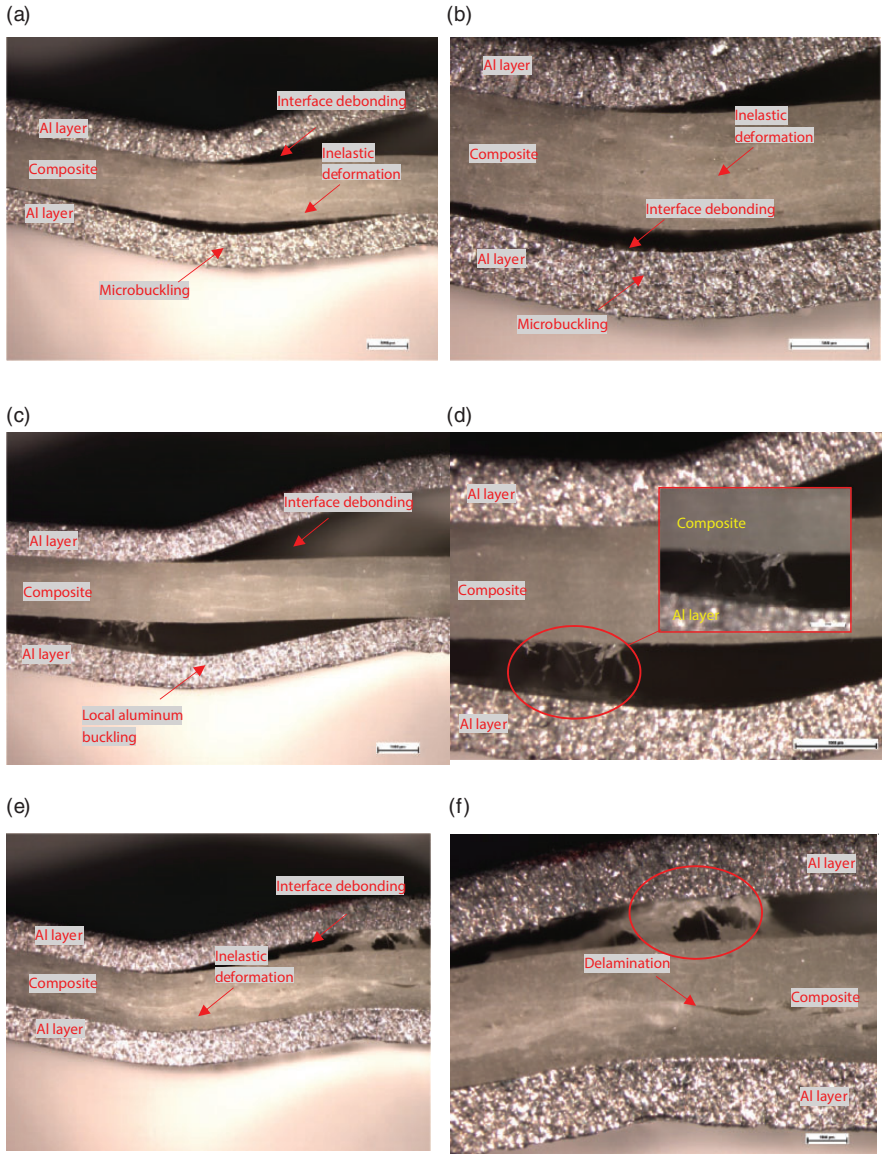**Figure 15.** Microscopic analysis of (a, b) reference FML, (c, d) 17-FML, and (e, f) 50-FML ILSS test specimens.

epoxide groups in epoxy resin. More detailed information regarding the chemical interactions between epoxy and nylon can be found in Gul et al. [49]. The chemical interactions improve the wetting efficiency and give a resin-rich surface which possibly arrests the crack initiation at the interface of the FMLs.
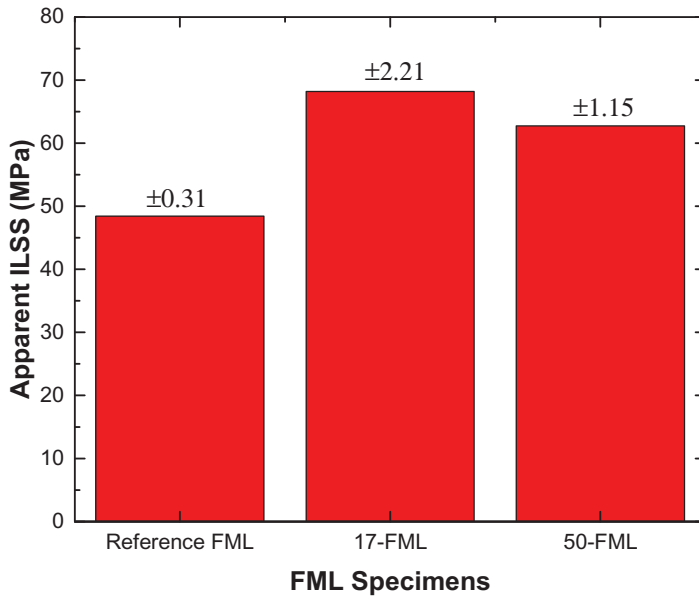
Figure 16. Short-beam strength values of FML test specimens.

Figure 11(d) to (f) shows the SEM images of ILSS specimens (side view) of PA 66 interleaved FMLs. The deformed PA 66 fibers which participate in load transfer are visible in Figure 11(d). The severe matrix deformation can be seen in Figure 11(d) to (f). It is obvious that the PA 66 interlayers increased the plastic deformation ability of brittle matrix. Also, hundreds of thousands of PA 66 micro-fibers in the interface of FMLs contribute load sharing process by deforming plastically which leads to significant increase in ILSS of FMLs. As previously stated, the reported value of ILSS for GLARE laminates is between 40 and 45 MPa in the literature [48]. However, the ILSS of CF/EP and EG/EP composites is more than twice (about 85 MPa) as compared to that of GLARE laminates. The results show that the PA 66 interlayers can be used as a secondary reinforcement for improving the ILSS of traditional FMLs. It is also noteworthy that the areal weight density is the key parameter which minimizes the trade-off between ILSS and in-plane mechanical properties of FMLs.

AE test results

The implementation of the DBSCAN clustering algorithm on the raw AE data yielded similar results for all FML samples. Thus, the results shown in Figure 17 are only provided for 50-FML specimens. Dataset for 50-FML bending and tensile specimens, given in Figure 17(a) and (c) respectively, shows low spatial density at the weighted peak frequency range below 300 kHz while high spatial density above
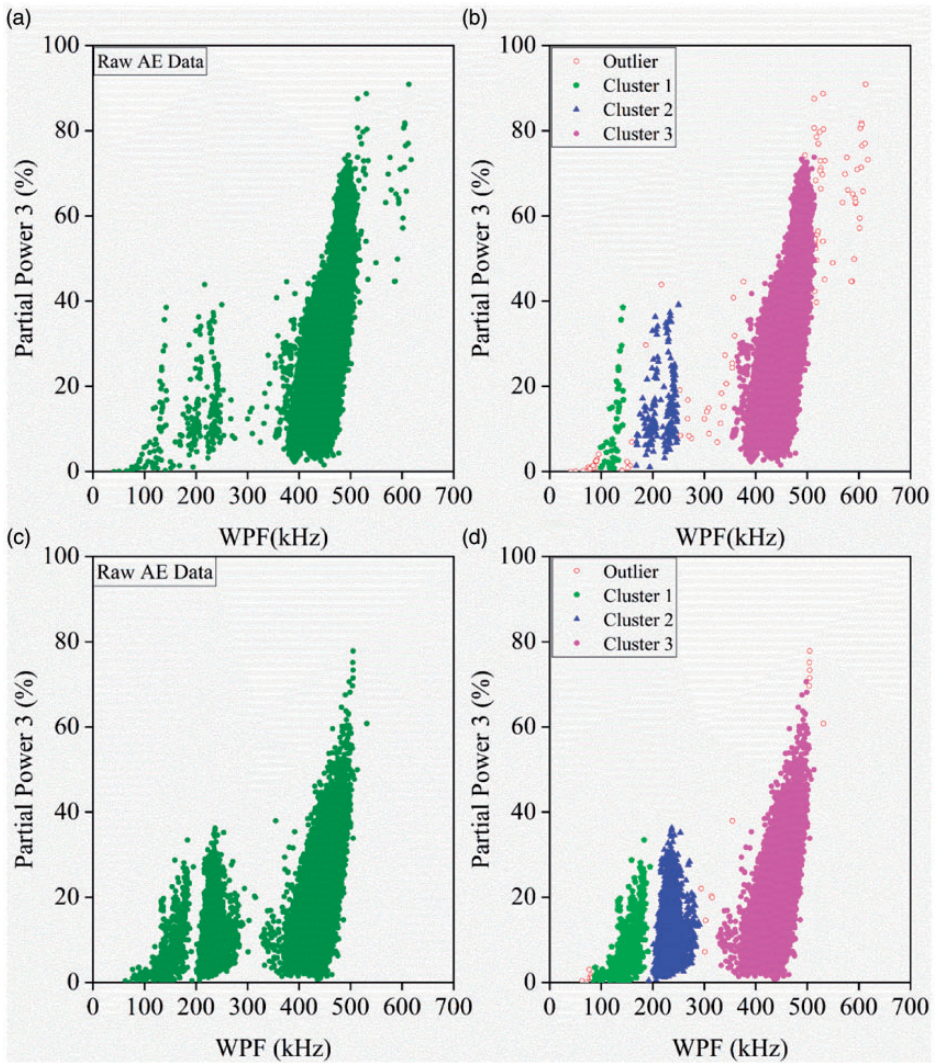
Figure 17. (a) Raw AE data for 50-FML bending; (b) clustered AE data for 50-FML bending; (c) raw AE data for 50-FML tensile; (d) clustered data for 50-FML tensile.

400 kHz. The same results are obtained for tensile tests as seen in Figure 17(d). Considering the spatial density variation throughout the feature space, the DBSCAN algorithm can be used to find out the correct number of the clusters as seen in Figure 17(b) and (d) without encountering the problem of unifying the distinct data set into a single cluster, which is a common issue in cluster algorithms based on the distance function. Three different clusters and outlier data set are

obtained as a result of the classification procedure for the bending and tensile samples. These three clusters will include the AE activities associated with composite section, aluminum face sheet, and interleaves. The composite section should involve AE hits due to matrix cracking, interface failure between the glass fiber, and the polymer matrix/the delamination between the plies and E-glass fiber breakage. The 2024 series aluminum alloy as a face sheet should have AE activities due to the plastic deformation and the failure of intermetallic particles, e.g. Al_2Cu and Al_2CuMg. The interleaf is expected to have AE activities arising from inter-fiber breakage due to reorientation of PA 66 randomly distributed micro-fibers and the micro-fiber fracture. Finally, there should be AE activities across the interface of composite section and aluminum face sheets. Referring to earlier detailed studies by the authors as well as the open literature on composite and aluminum alloys individually, one can see that the first and the second clusters spanning from 100 to 200 kHz and 200 and 300 kHz should include the AE activity related to the matrix cracking and the damage formation at the interface of E-glass fiber-polymer matrix, respectively [30]. Furthermore, the first and the second clusters should also contain the AE activity due to plastic deformation of aluminum face sheets [50,51]. The third cluster obtained for the highest weighted peak frequency range of 350–500 kHz contains activities due to E-glass fiber breakage [32,36] and the failure of intermetallic particles, e.g. Al_2Cu and Al_2CuMg, in 2024 aluminum alloys. As reported by Wisner et al. [51], failure of these intermetallic particles results in peak frequency between 400 and 550 kHz. This range for the peak frequency matches with the weighted peak frequency range of 350–550 kHz for the third cluster in this study.

The failure analysis of nonwoven fabric tensile tests shows that for 17 gsm fabrics, the failure region is away from the middle of the gauge length and the AE sensor position, while for all 50gsm specimens, the failure occurs in the pre-determined path between edge notches. According to an investigation by Ridruejo et al. [52], two main types of damages can occur in nonwoven fabrics, namely inter-fiber breakage and micro-fiber fracture. The failure progress of the 17 gsm samples shows a considerable reorientation of fibers leading to inter-fiber breakage and consequently gradual separation of fibers away from sensor position. However, for 50-gsm interleaf, the damage is mainly in the form of fiber fracture-induced crack growth between edge notches normal to loading direction and includes negligibly small amount of fiber reorientation. Two main ranges of weighted peak frequency are observed for these samples, namely, 200–250 and 350–450 kHz. The later range is not visible for 17 gsm fabrics, thereby pointing to the absence of major micro-fiber fracture due to the separation of fibers but the presence of fiber reorientation. To this end, it can be prudently suggested that the range between 200 and 250 kHz is owing to the inter-fiber breakage of nonwoven fabric. Eventually, the second range which appears significantly for 50 gsm samples is related to micro-fiber fractures. These weighted peak frequency ranges for nonwoven fabric failure fall into the second and the third clusters of AE data, respectively, for 17-FML and 50-FML samples and contribute to the number of hits in these clusters.

Table 2. Percentage of hits for each cluster.

Sample	Bending				Tensile			
	Outlier (%)	Cluster 1 (%)	Cluster 2 (%)	Cluster 3 (%)	Outlier (%)	Cluster 1 (%)	Cluster 2 (%)	Cluster 3 (%)
Ref-FML	0.04	0.07	0.12	99.77	0.39	46.83	25.69	27.08
17-FML	0.20	0.19	11.23	88.38	3.39	18.72	30.59	47.30
50-FML	0.16	0.08	0.31	99.45	0.12	3.74	28.25	67.89

It is observed that about 99.45% of all AE hits given in Figure 16(b) is related to the third cluster. This result is notably different from that of authors about AE analysis on polymer composites under flexural loading in terms of the number of hits for high frequency failure modes (fiber breakage), i.e. 70% [30]. This difference can be explained by referring three main contributions, namely, failure of the intermetallic particles in aluminum alloy, nonwoven micro-fiber breakage, and the inability to record the AE activity as result of sudden debonding between aluminum face sheets and composite section under bending loading condition. Table 2 shows the percentage of AE hits obtained for each sample under bending and tensile loading conditions. It is seen that for the reference FML sample, about 99.77% of AE hits are in the third cluster; while for 17-FML specimen, this value decreases down to 88.38%. Again for 17-FML specimen, the percentage of activity for the first and the second cluster has risen from 0.07 to 0.19% and 0.12 to 11.23%, respectively, with respect to the reference FML sample. These changes might be explained through two possible reasons. The first one is that a better adhesion between the aluminum face sheet and the composite section due to the interleaf is achieved, thereby preventing possible debonding therein. The better adhesion consequently enables the AE activities belonging to the first and the second cluster to be recorded by the sensors. The second one is the implication that the interface failure between aluminum and composite section occurs in the weighted peak frequency range between 200 and 300 kHz. Regardless of these two possible reasons, it is obvious that the interface between aluminum and composite section is modified in terms of the failure modes due to the presence of PA66 interleaves. As for the 50-FML sample, the percent of AE hits for the first cluster does not change notably while that for the second cluster, it raises up to 0.31% with respect to the reference FML. This variation of AE hits indicates that both thicker and denser interleave does not affect the aluminum-composite section interface as much as in the case of 17-FML sample. Thicker interleaving prevents easy reorientation of nonwoven fibers under flexural loading, therefore encouraging their fracture, i.e. revealing itself as an increase in the number of hits in the third cluster between 350 and 450 kHz and a consequent reduction in the number of hits in the second cluster between 250 and 300 kHz.

As given in Table 2, there appears to be an inverse relation between the number of hits in the first and the third clusters under tensile loading condition.

Table 3. Weighted peak frequency range for each failure type.

Weighted peak frequency range (kHz)	Failure type
100–200	Composite section matrix cracking–aluminum plastic deformation
200–300	Composite section interface failure, aluminum plastic deformation, and nonwoven fabric interfiber breakage
350–500	Composite section fiber breakage, interface failure, and nonwoven fabric fiber fracture

For 50-FML, where the thickness and the density of the interleave is the highest, the percentage of AE hits in the first and the third clusters, respectively, decreases significantly from 46.83% to 3.74% and surges up from 27.08 to 67.89% with respect to the reference FML. The notable variation in the number of hits for the first and the third clusters for both 17-and 50-FML with respect to the reference FML obviously indicates that the first and the third clusters are highly related to the matrix cracking and fiber failure. It is also noted from the table that there are no drastic changes in the number of hits for the second cluster for 17-FML and 50-FML with respect to the reference FML, indicating that the second cluster is mainly associated with the interface damage phenomenon because the tensile load is not affecting the interface unlike the flexural load. This AE result is consistent with the observations of featureless and smooth surfaces seen in Figure 10. Recalling from "Mechanical test results and fractured surface observations" section, the nonwoven fabric toughens the matrix material through formation of semi-IPN. Moreover, the load transfer from aluminum face sheets to composite section is improved due to the presence of interleaves. The reduction of AE hits in the first cluster can be related to toughened matrix material which hinders crack initiation and growth. Consequently, the matrix transfers the load to reinforcing E-glass fibers, and as the load increases, the fiber rupture starts, thereby leading to a rise in the hits of the third cluster. The increase in number of hits for the second cluster in 17-FML tensile sample compared to reference FML can be attributed to the incorporation of nonwoven fibers reorientation, i.e. interfiber breakage. This fiber reorientation capability is surpassed due to higher density of fibers in 50-FML sample and causes slight drop in number of the hits to 28.25% which is close to the level of the reference FML, 25.69%. Thus, the range of weighted peak frequencies and their related failure types can be given as in Table 3.

Figure 18 shows the change in stress level of tested samples and their corresponding number of AE counts over time. The quantity of the AE counts shows the number of times in which the energy level of acoustic wave has crossed the threshold. Thus, this parameter is directly related to the energy dissipation through AE waves due to the damage propagation inside material. Generally, in all flexural samples, the AE activity gets significantly populated toward the final stages of the test and attains its maximum value corresponding to the first stress drop point.
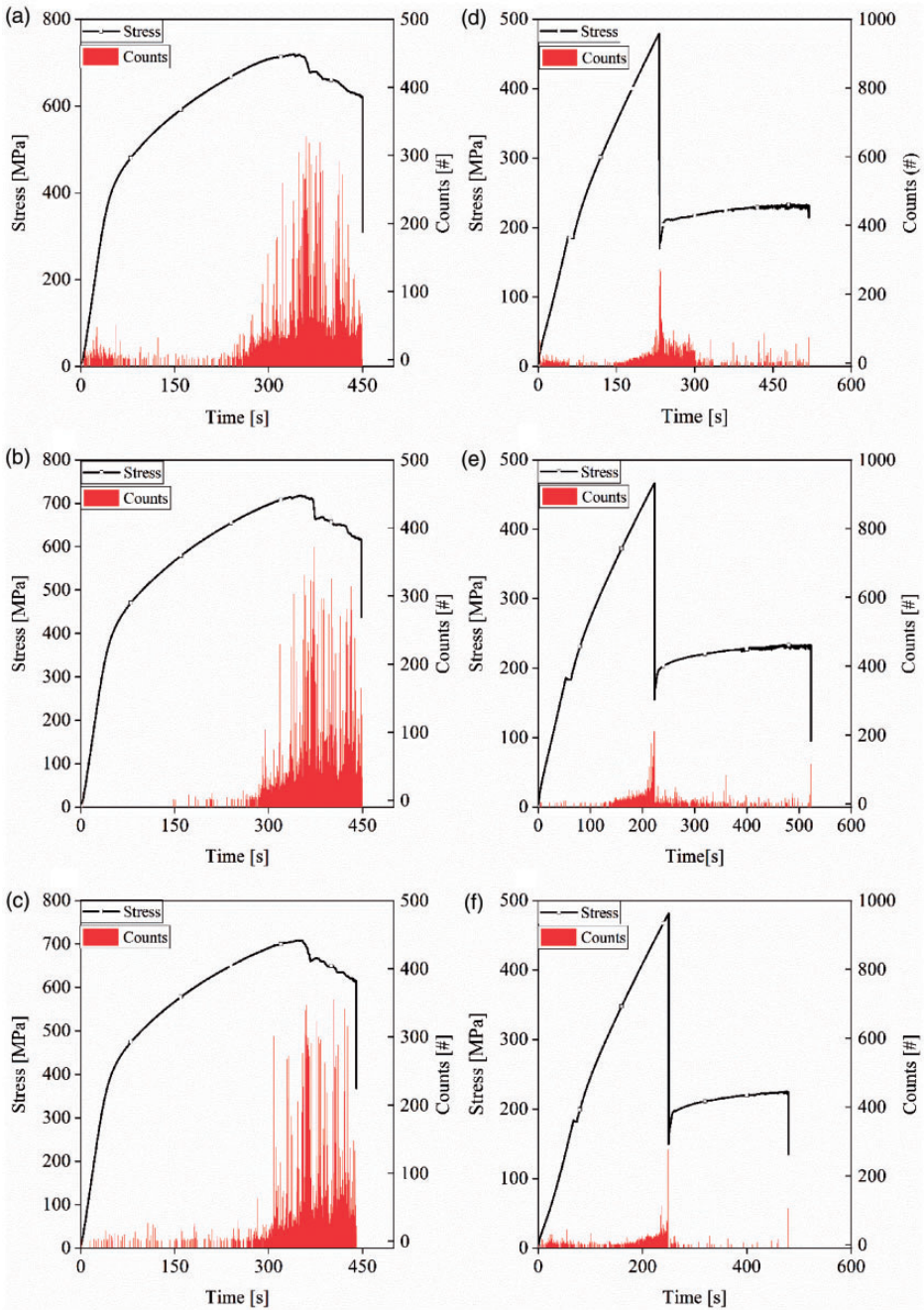
Figure 18. Stress–time–AE activity plot for (a) reference FML, (b) 17-FML, (c) 50-FML under three-point bending, (d) reference FML, (e) 17-FML, and (f) 50-FML under tension test.

Then, the material continues to withstand the load until the global failure occurs, and the number of counts at final failure stress is not higher than the maximum value obtained at maximum stress level. As seen in Figure 18(a), for the reference FML, there exists significant amount of acoustic activity in the linear region of the graph, whereas same region shows less activity for 50-FML in Figure 18(c) and almost a negligible activity for 17-FML specimen, Figure 18(b). This observation can be related to easier reorientation of nonwoven fibers at interlayer for 17-FML sample as they rearrange efficiently under flexural loading, whereas for reference and 50-FML samples, this reorientation is not possible and hard, respectively, which promotes interface failure between aluminum and composite section in addition to matrix cracking. Moreover, this initial activity happens immediately after the start of the test which is at elastic region for the reference FML and 50-FML samples. According to Bussiba et al. [37], the presence of AE activity in the elastic region and its variation corresponds to detachment and split of metal layers from polymeric material. Thus, it is evident that the density of interleaving has a direct effect on the propagation rate of interface failure between metal and composite section.

Figure 18(d) to (f) shows the variation of the stress as a function of time throughout tensile tests for various samples, where the first drops in the stress level are related to the rupture in the composite section while the remaining part is related to plastic deformation of aluminum face sheets. Considering that, after the failure of composite section, aluminum sheets will be the only load carriers, and the AE activity will be only due to plastic deformation of aluminum and detachment of aluminum face sheets from the composite section. It is seen that the AE activity decreased for 17-FML and 50-FML samples with respect to the reference sample. As previously mentioned in Figure 10, the plastic deformability of matrix increases with the presence of interleaving, which hinders interface failure between aluminum and composite section. This effect becomes very important in tensile test after the failure of composite section as it is more prone to splitting between different section of laminates structure, namely aluminum and composite section. These AE activity plots show that using AE activity charts can reveal the effect of PA 66 interface modification on failure behavior of FMLs under different loading conditions.

Table 4. The impact characteristics of reference and PA 66 interleaved FMLs.

Sample	Max force (N)	Peak energy (J)	Time (ms)
Ref-FML	10087 ± 153	57.23 ± 3.25	8.66 ± 0.14
17-FML	10272 ± 133	58.50 ± 0.75	8.58 ± 0.02
50-FML	10133 ± 137	56.35 ± 2.43	8.87 ± 0.28

(a) Reference

Debonded length=63.4 mm

Interface debonding

Transverse cracks and fiber breakage

Plastic deformation and aluminum failure

Interface debonding

(b) 17-FML

Debonded length=42.8 mm

Transverse cracks and fiber breakage

Interface debonding

Plastic deformation and aluminum failure

(c) 50-FML

Debonded length=38.5 mm

Transverse cracks and fiber breakage

Interface debonding

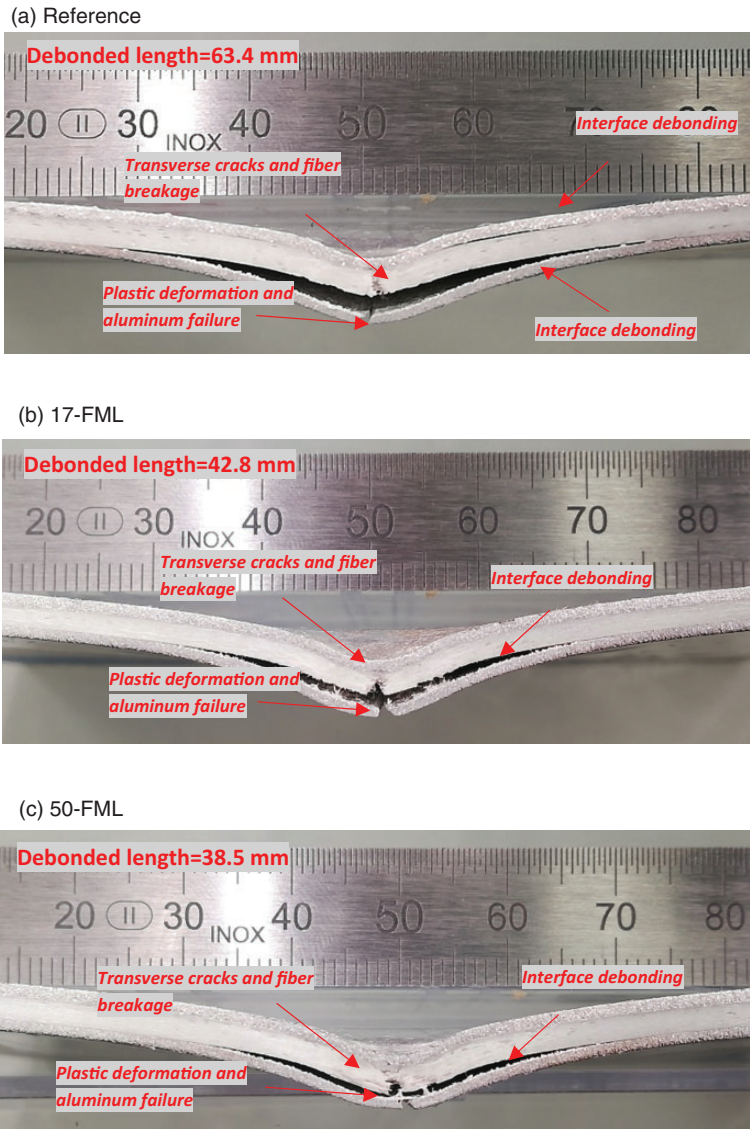Plastic deformation and aluminum failure

Figure 19. Cross-sectional view of impacted FML specimens.

Low-velocity impact test results

Table 4 summarizes the impact characteristics of the reference and PA 66 interleaved FML specimens. It is observed that the impact response is not influenced by the presence of PA 66 interlayers in terms of peak force, energy, and time values.
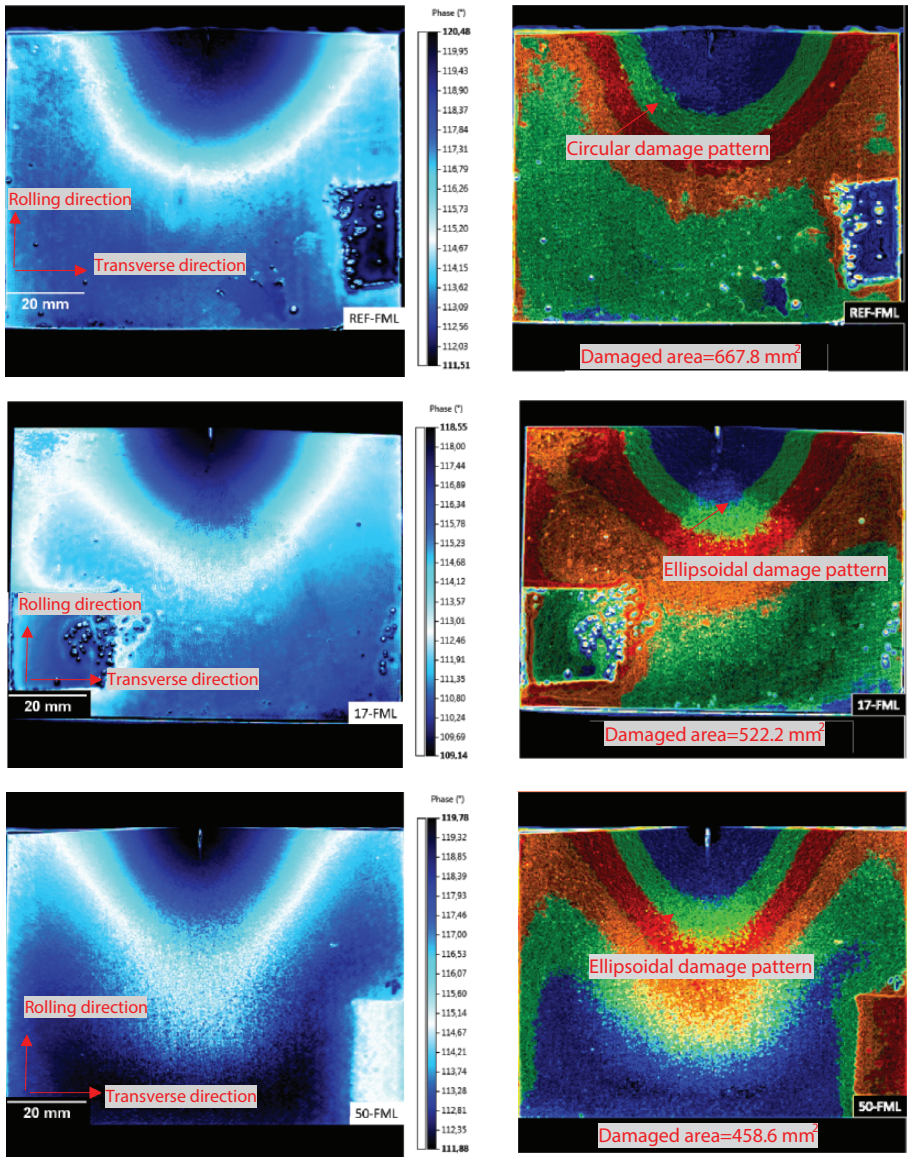
Figure 20. Thermal images of impacted FML specimens.

This result is similar to that of obtained by Zarei et al. [4] and Akangah et al. [24]. They showed that the PA 66 nanofiber interleaving had no significant effect on the peak force, energy, and time values of GLARE laminates. Nevertheless, we have shown that the presence of PA 66 interlayers significantly affects the debonded

length and damaged area. The cross-sectional view of the impacted FML speci-
mens is shown in Figure 19, where one can observe four different failure modes in
the specimens, namely, extensive delamination, transverse cracks, and fiber break-
age in composite layers and failure of bottom aluminum layer. It is important to
note that the interface debonding between top aluminum layer and composite
section is vanished in the PA 66 interleaved specimens due to the improved adhe-
sion between aluminum and composite sections. The debonded length of the
impacted FML specimens was determined to be 63.4, 42.8, and 38.5 mm for the
reference FML, 17-FML, and 50-FML specimens, respectively, by using Image J
software. This corresponds to a decrease in the debonded length about 32 and 39%
for 17 and 50 gsm areal weight densities, respectively. Figure 20 shows the phase
maps achieved through lock in thermography. As can be seen in this figure, the
reference-FML specimens have a circular damage pattern which is one of the main
characteristics of low interlaminar fracture toughness [23–24]. The circular damage
pattern indicates that the delamination in the reference FML specimens propagates
in both rolling and transverse directions of aluminum face sheet due to impact
loading. It is noteworthy that the addition of PA 66 interlayers into the reference
FML alters the damage pattern from circular shape to the ellipsoidal one. This
clearly indicates that the presence of PA 66 interlayers improves the fracture
toughness of the reference FML specimens. The thermal images are processed
with Image J software to determine the damaged area of the FML specimens.
The damaged area of the reference FML, 17-FML, and 50-FML specimens is
determined to be 667.8, 522.2, and 458.6 mm^2, respectively. The addition of PA
66 interlayers reduces the damaged area about 22 and 32% for 17 and 50 gsm areal
weight densities, respectively.

Concluding remarks

This study sheds light on the effects of PA 66 interlayers on the failure modes and
mechanical performance of FMLs made of E-glass fiber/epoxy and aluminum face
sheets. Tensile, three-point bending, ILSS, and low-velocity impact tests are car-
ried out on the reference and PA 66 interleaved FMLs in accordance with relevant
ASTM standards. AE technique is used for in-situ monitoring of FMLs with/
without PA 66 interlayers under different loading conditions. The following results
can be drawn:

- The tensile and flexural test results indicate that the PA 66 interlayers had no
  statistically significant effect on the tensile and flexural modulus of the FMLs. A
  small decrease in the range of 3–6% is observed in the tensile and flexural
  moduli of the FMLs.
- It is shown that the PA 66 interlayers improve ILSS values of the FMLs sig-
  nificantly about 42%.

- Impact test results indicate that the PA 66 interlayers lead to significant reduction in the debonded length and damaged area by about 39 and 32%, respectively.
- Optical and SEM observations show that the plastic deformation ability of epoxy matrix and the load transfer efficiency is improved with the presence of PA 66 interlayers.
- The AE activity charts can reveal the effect of PA 66 interface modification on failure behavior of the FMLs under different loading conditions.

Declaration of Conflicting Interests

Funding

ORCID iD

Mehmet Yildiz ⓘ https://orcid.org/0000-0003-1626-5858

References

1. Roebroeks G. Fibre-metal laminates: recent developments and applications. *Int J Fatigue* 1994; 16: 33–42.
2. Wu G and Yang J. The mechanical behavior of GLARE laminates for aircraft structures. *JOM* 2005; 57: 72–79.
3. Vogelesang LB and Vlot A. Development of fibre metal laminates for advanced aerospace structures. *J Mater Process Technol* 2000; 103: 1–5.
4. Zarei H, Brugo T, Belcari J, et al. Low velocity impact damage assessment of GLARE fiber-metal laminates interleaved by Nylon 6,6 nanofiber mats. *Compos Struct* 2017; 167: 123–131.
5. Sinmazçelik T, Avcu E, Bora OM, et al. A review: fibre metal laminates, background, bonding types and applied test methods. *Mater Des* 2011; 32: 3671–3685.
6. Chandrasekar M, Ishak M, Jawaid M, et al. An experimental review on the mechanical properties and hygrothermal behaviour of fibre metal laminates. *J Reinf Plast Comp* 2017; 36: 72–82.
7. Sadighi M, Alderliesten RC and Benedictus R. Impact resistance of fiber-metal laminates: a review. *Int J Impact Eng* 2012; 49: 77–90.
8. Sharma AP, Khan SH and Parameswaran V. Experimental and numerical investigation on the uni-axial tensile response and failure of fiber metal laminates. *Compos Part B-Eng* 2017; 125: 259–274.
9. Mathivanan P, Balakrishnan M and Krishnan H. Metal thickness, fiber volume fraction effect on the tensile properties, debonding of hybrid laminates. *J Reinf Plast Comp* 2010; 29: 2128–2140.

10. Reyes VG and Cantwell WJ. The mechanical properties of fibre-metal laminates based on glass fibre reinforced polypropylene. *Compos Sci Technol* 2000; 60: 1085–1094.

11. Du D, Hu Y, Li H, et al. Open-hole tensile progressive damage and failure prediction of carbon fiber-reinforced PEEK-titanium laminates. *Compos Part B-Eng* 2016; 91: 65–74.

12. Li H, Xu Y, Hu X, et al. Bending failure mechanism and flexural properties of GLARE laminates with different stacking sequences. *Compos Struct* 2018; 187: 354–363.

13. Hinz S, Omoori T, Hojo M, et al. Damage characterisation of fibre metal laminates under interlaminar shear load. *Compos Part A-Appl S* 2009; 40: 925–931.

14. Hinz S, Heidemann J and Schulte K. Damage evaluation of Glare® 4B under inter-laminar shear loading at different temperature conditions. *Adv Compos Lett* 2005; 14: 47–55.

15. Liu C, Du D, Li H, et al. Interlaminar failure behavior of GLARE laminates under short-beam three-point-bending load. *Compos Part B-Eng* 2016; 97: 361–367.

16. Zhang J, Chaisombat K, He S, et al. Hybrid composite laminates reinforced with glass/carbon woven fabrics for lightweight load bearing structures. *Mater Des* 2012; 36: 75–80.

17. Beylergil B, Tanoglu M and Aktas E. Enhancement of interlaminar fracture toughness of carbon fiber-epoxy composites using polyamide-6,6 electrospun nanofibers. *J Appl Polym Sci* 2017; 134:45244.

18. Beylergil B, Tanoglu M and Aktas E. Effect of polyamide-6,6 (PA 66) nonwoven veils on the mechanical performance of carbon fiber/epoxy composites. *Compos Struct* 2018; 194: 21–35.

19. Quan D, Mischo C, Li X, et al. Improving the electrical conductivity and fracture toughness of carbon fibre/epoxy composites by interleaving MWCNT doped thermo-plastic veils. *Compos Sci Technol* 2019; 182: 107775.

20. Beylergil B, Tanoglu M and Aktas A. Modification of carbon fibre/epoxy composites by polyvinyl alcohol (PVA) based electrospun nanofibers. *Adv Compos Lett* 2016; 25: 69–76.

21. Beylergil B, Tanoglu M and Aktas A. Mode-I fracture toughness of carbon fiber/epoxy composites interleaved by aramid nonwoven veils. *Steel Compos Struct* 2019; 31: 113–123.

22. Lee SH, Noguchi H, Kim YB, et al. Effect of interleaved non-woven carbon tissue on interlaminar fracture toughness of laminated composites, part I: mode II. *J Compos Mater* 2002; 36: 2153–2168.

23. Palazzetti R, Zucchelli A and Trendafilova I. The self-reinforcing effect of Nylon 6,6 nano-fibres on CFRP laminates subjected to low velocity impact. *Compos Struct* 2013; 106: 661–671.

24. Akangah P, Lingaiah S and Shivakumar K. Effect of Nylon-66 nano-fiber interleaving on impact damage resistance of epoxy/carbon fiber composite laminates. *Compos Struct* 2010; 92: 1432–1439.

25. Paipetis AS and Aggelis DG. Damage Assessment in fibrous composites using acoustic emission, acoustic emission, Wojciech Sikorski, IntechOpen, www.intechopen.com/books/acoustic-emission/damage-assessment-in-fibrouscomposites-using-acoustic-emis sion (2012, accessed 16 April 2020).

26. Ramirez-Jimenez CR, Papadakis N, Reynolds N, et al. Identification of failure modes in glass/polypropylene composites by means of the primary frequency content of the acoustic emission event. *Compos Sci Technol* 2004; 64: 1819–1827.

27. Sause MGR, Gribov A, Unwin AR, et al. Pattern recognition approach to identify natural clusters of acoustic emission signals. *Pattern Recogn Lett* 2012; 33: 17–23.

28. Flament C, Salvia M, Berthel B, et al. Local strain and damage measurements on a composite with digital image correlation and acoustic emission. *J Compos Mater* 2016; 50: 1989–1996.

29. Oz FE, Ersoy N, Mehdikhani M, et al. Multi-instrument in-situ damage monitoring in quasi-isotropic CFRP laminates under tension. *Compos Struct* 2018; 196: 163–180.

30. Tabrizi IE, Kefal A, Zanjani JSM , et al. Experimental and numerical investigation on fracture behavior of glass/carbon fiber hybrid composites using acoustic emission method and refined zigzag theory. *Compos Struct* 2019; 223: 110971.

31. Bohmann T, Schlamp M and Ehrlich I. Acoustic emission of material damages in glass fibre-reinforced plastics. *Compos Part B-Eng* 2018; 155: 444–451.

32. Yilmaz C and Yildiz M. A study on correlating reduction in Poisson's ratio with transverse crack and delamination through acoustic emission signals. *Polym Test* 2017; 63: 47–53.

33. Pawar OA, Gaikhe YS, Tewari A, et al. Analysis of hole quality in drilling GLARE fiber metal laminates. *Compos Struct* 2015; 123: 350–365.

34. Al-Azzawi ASM, McCrory J, Kawashita LF, et al. Buckling and postbuckling behaviour of Glare laminates containing splices and doublers, part 1: instrumented tests. *Compos Struct* 2017; 176: 1158–1169.

35. Ammar IB, Karra C, El Mahi A, et al. Mechanical behavior and acoustic emission technique for detecting damage in sandwich structures. *Appl Acoust* 2014; 86: 106–117.

36. Pashmforoush F, Khamedi R, Fotouhi M, et al. Damage classification of sandwich composites using acoustic emission technique and k-means Genetic Algorithm. *J Nondestruct Eval* 2014; 33: 481–492.

37. Bussiba A, Kubiec M, Ifergane S, et al. Damage evolution and fracture events sequence in various composites by acoustic emission technique. *Compos Sci Technol* 2008; 68: 1144–1155.

38. ASTM D2344. *In annual book of ASTM standards*. Philadelphia, PA: American Society for Testing and Materials, 2013.

39. ASTM D790-10. *In annual book of ASTM standards*. Philadelphia, PA: American Society for Testing and Materials, 2010.

40. ASTM D3039/D3039M-17. *Standard test method for tensile properties of polymer matrix composite materials*. West Conshohocken, PA: ASTM International, 2017.

41. De Baere I, Van Paepegem W, Quaresimin M, et al. On the tension–tension fatigue behaviour of a carbon reinforced thermoplastic, part I: limitations of the ASTM D3039/D3479 standard. *Polym Test* 2011; 30: 625–632.

42. De Baere I, Van Paepegem W, Hochard C, et al. On the tension–tension fatigue behaviour of a carbon reinforced thermoplastic, part II: evaluation of a dumbbell-shaped specimen. *Polym Test* 2011; 30: 663–672.

43. Ester M, Kriegel HP, Sander J, et al. A density-based algorithm for discovering clusters in large spatial databases with noise. In: E. Simoudis, J. Han, and U Fayyad (Eds.), *KDD'96: proceedings of the second international conference on knowledge discovery and data mining*, 1996, pp. 226–231.

44. Tran TN, Drab K and Daszykowski M. Revised DBSCAN algorithm to cluster data with dense adjacent clusters. *Chemometr Intell Lab* 2013; 120: 92–96.

45. Rajkumar GR, Krishna M, Narasimhamurthy HN, et al. Investigation of tensile and bending behavior of aluminum based hybrid fiber metal laminates. *Proc Mater Sci* 2014; 5: 60–68.
46. Zanjani JSM, Okan BS, Letofsky-Papst I, et al. Repeated self-healing of nano and micro scale cracks in epoxy-based composites by tri-axial electrospun fibers including different healing agents. *RSC Adv* 2015; 5: 73133–73145.
47. Khalili SML, Daghigh V and Farsani RE. Mechanical behavior of basalt fiber-reinforced and basalt fiber metal laminate composites under tensile and bending loads. *J Reinf Plast Comp* 2011; 30: 647–659.
48. Botelho EC, Silva RA, Pardini LC, et al. A review on the development and properties of continuous fiber/epoxy/aluminum hybrid composites for aircraft structures. *Mat Res* 2006; 9: 247–256.
49. Gul S, Kausar A, Mehmood M, et al. Progress on epoxy/polyamide and inorganic nanofiller-based hybrids: introduction, application, and future potential. *Polym Plast Technol* 2016; 55: 1842–1862.
50. Jiang J, Ye C, Zhang Z, et al. Acoustic emission testing on aluminum alloy pressure vessels. In: Shen G, Wu Z and Zhang J (Eds.), *Advances in acoustic emission technology. Springer proceedings in physics.* Cham: Springer, 2017, pp.179.
51. Wisner B, Mazur K, Perumal V, et al. Acoustic emission signal processing framework to identify fracture in aluminum alloys. *Eng Fract Mech* 2019; 210: 367–380.
52. Ridruejo A, Gonzalez C and Llorka JI. Micromechanisms of deformation and fracture of polypropylene nonwoven fabrics. *Int J Solids Struct* 2011; 48: 153–162.